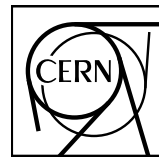


EUROPEAN ORGANIZATION FOR NUCLEAR RESEARCH



CERN-EP-2023-176
22 August 2023

$K^*(892)^\pm$ resonance production in Pb–Pb collisions at $\sqrt{s_{\text{NN}}} = 5.02 \text{ TeV}$

ALICE Collaboration*

Abstract

The production of $K^*(892)^\pm$ meson resonance is measured at midrapidity ($|y| < 0.5$) in Pb–Pb collisions at $\sqrt{s_{\text{NN}}} = 5.02 \text{ TeV}$ using the ALICE detector at the Large Hadron Collider. The resonance is reconstructed via its hadronic decay channel $K^*(892)^\pm \rightarrow K_0^0 \pi^\pm$. The transverse momentum distributions are obtained for various centrality intervals in the p_T range of 0.4 – $16 \text{ GeV}/c$. Measurements of integrated yields, mean transverse momenta, and particle yield ratios are reported and found to be consistent with previous ALICE measurements for $K^*(892)^0$ within uncertainties. The p_T -integrated yield ratio $2K^*(892)^\pm/(K^+ + K^-)$ in central Pb–Pb collisions shows a significant suppression at a level of 9.3σ relative to pp collisions. Thermal model calculations result in an over-prediction of the particle yield ratio. Although both HRG-PCE and MUSIC+SMASH simulations consider the hadronic phase, only HRG-PCE accurately represents the measurements, whereas MUSIC+SMASH simulations tend to overpredict the particle yield ratio. These observations, along with the kinetic freeze-out temperatures extracted from the yields measured for light-flavored hadrons using the HRG-PCE model, indicate a finite hadronic phase lifetime, which decreases with increasing collision centrality percentile. The p_T -differential yield ratios $2K^*(892)^\pm/(K^+ + K^-)$ and $2K^*(892)^\pm/(\pi^+ + \pi^-)$ are presented and compared with measurements in pp collisions at $\sqrt{s} = 5.02 \text{ TeV}$. Both particle ratios are found to be suppressed by up to a factor of five at $p_T < 2.0 \text{ GeV}/c$ in central Pb–Pb collisions and are qualitatively consistent with expectations for rescattering effects in the hadronic phase. The nuclear modification factor (R_{AA}) shows a smooth evolution with centrality and is found to be below unity at $p_T > 8 \text{ GeV}/c$, consistent with measurements for other light-flavored hadrons. The smallest values are observed in most central collisions, indicating larger energy loss of partons traversing the dense medium.

© 2023 CERN for the benefit of the ALICE Collaboration.

Reproduction of this article or parts of it is allowed as specified in the CC-BY-4.0 license.

*See Appendix A for the list of collaboration members

1 Introduction

The primary goal of ultra-relativistic heavy-ion collisions is to map the phase diagram of Quantum Chromodynamics (QCD) and to investigate the properties of the strongly-interacting matter at extreme conditions of high temperatures and net baryon densities. At RHIC and LHC energies, compelling evidence for the formation of a strongly-interacting quark–gluon plasma (QGP), where quarks and gluons are the primary degrees of freedom, has been observed [1–15]. Hydrodynamic models provide successful descriptions of the evolution of the QGP by assuming local thermal equilibrium and specific initial conditions [16–26]. As the system expands and cools down to the hadronization temperature [27, 28], the quark–gluon plasma turns into colorless hadrons in the process known as hadronization [29–32]. After the hadronization, the system reaches a certain temperature called the chemical freeze-out temperature [33], where the inelastic collisions among the hadrons cease, and the yields of stable particles become fixed [34, 35]. After the chemical freeze-out, the hadrons continue to interact among themselves via elastic scattering, which can further modify the yields and shapes of their transverse momentum spectra. Later, the system reaches a stage when the mean free path of the hadrons becomes much larger than the system size, known as kinetic freeze-out [35] after which the hadrons stream freely to the detectors. As the chemical freeze-out and quark-hadron transition temperatures are close by, the phase between chemical and kinetic freeze-out is called here as the hadronic phase [27, 28, 36]. The dynamics of this hadronic phase can be probed by the measurements of hadronic decays of short-lived resonances. The decay products of the resonances inside the hadronic phase take part in two simultaneous processes called regeneration and rescattering via elastic or pseudoelastic scattering (scattering through an intermediate state), which can result in modification of the measured resonance yields [37, 38]. If at least one of the decay products scatters elastically with other hadrons in the hadronic medium or pseudoelastically scatters via a different resonance state (e.g. a pion from K^{*}(892)[±] decay scatters with another pion in the hadronic medium, $\pi^-\pi^+ \rightarrow \rho^0 \rightarrow \pi^-\pi^+$), the four-momentum information about the parent resonance gets lost and the particle can no longer be reconstructed. On the other hand, pseudoelastic scatterings among the hadrons inside the medium can regenerate the resonance state (eg. $K_S^0\pi^\pm \rightarrow K^*(892)^\pm \rightarrow K_S^0\pi^\pm$) which can lead to an increase in resonance yield. The strength of these two processes depends on the hadronic phase lifetime, density of the hadronic medium, hadronic interaction cross section of decay products of the resonances, and the lifetime of resonances. The dominance of one effect over the other can be investigated by studying the yield ratios of resonances to longer-lived hadrons with the same quark content as a function of the collision centrality.

The K^{*}(892)⁰ and $\phi(1020)$ meson resonances have been measured previously in various collision systems [39–52]. The K^{*}(892)⁰ resonance has a lifetime of about 4.16 fm/c, which is comparable to that of the hadronic phase lifetime [39, 51, 53] and decays predominantly to $K^*(892)^0 \rightarrow K^\mp\pi^\pm$, whereas the ϕ meson has a longer lifetime of about 46.3 fm/c decaying as $\phi \rightarrow K^+K^-$. Due to the smaller lifetime of the K^{*}(892)⁰ resonance, it can decay inside the hadronic medium. As a result, the decay daughters are expected to take part in rescattering and regeneration processes between chemical and kinetic freeze-out, which can alter the reconstructible yield of K^{*}(892)⁰. In contrast, the yield of the $\phi(1020)$ meson is anticipated to be largely unaffected by rescattering effects due to its significantly longer lifetime compared with the hadronic phase. Specifically, its lifetime differs from that of the K^{*}(892)⁰ by a factor of ten. However, its yield can be enhanced by the regeneration of kaons inside the hadronic medium. If rescattering dominates over regeneration, one would observe a reduction of the K^{*}(892)⁰ yield with respect to the longer-lived hadron yields with increasing system size, defined by collision centrality. Indeed in Refs. [39, 40, 43, 51], the integrated yield ratio $2K^*(892)^0/(K^+ + K^-)$ decreases with increasing system size suggesting the dominance of rescattering over regeneration in the hadronic phase of heavy-ion collisions. The study of p_T -differential particle ratios shows that the observed suppression occurs in the range of small transverse momenta, $p_T < 2$ GeV/c [54]. In contrast, $2\phi(1020)/(K^+ + K^-)$ ratio remained fairly constant as a function of centrality, ruling out a significant contribution of the regeneration effect

for $\phi(1020)$ meson.

In high-energy heavy-ion collisions, the high- p_{T} partons lose their energy while traversing the medium leading to jet quenching [6], manifesting itself in a suppressed production of high- p_{T} hadrons. The suppression is quantified using the nuclear modification factor (R_{AA}), defined as

$$R_{\text{AA}} = \frac{1}{\langle T_{\text{AA}} \rangle} \frac{d^2N^{\text{AA}}/(dydp_{\text{T}})}{d^2\sigma^{\text{pp}}/(dydp_{\text{T}})}, \quad (1)$$

where $d^2N^{\text{AA}}/(dydp_{\text{T}})$ is the particle yield in heavy-ion collisions, $d^2\sigma^{\text{pp}}/(dydp_{\text{T}})$ is the production cross section of the particle in pp collisions, $\langle T_{\text{AA}} \rangle = \langle N_{\text{coll}} \rangle / \sigma_{\text{inel}}$ is the average nuclear overlap function, $\langle N_{\text{coll}} \rangle$ is the average number of binary nucleon–nucleon collisions obtained from MC Glauber simulations [55] and σ_{inel} is the inelastic pp cross section [56]. The R_{AA} measurements in Pb–Pb collisions at $\sqrt{s_{\text{NN}}} = 5.02$ TeV and 2.76 TeV [39, 40, 57, 58] show that at high p_{T} (> 8 GeV/c) the nuclear modification factor for all light-flavored hadrons, including K^{*}(892)⁰ are consistent with each other, signifying flavor-independence of parton energy loss in the QGP.

In this article, the first measurement of K^{*}(892)[±] mesons at midrapidity, $|y| < 0.5$, in the transverse momentum range from 0.4 to 16 GeV/c in Pb–Pb collisions at $\sqrt{s_{\text{NN}}} = 5.02$ TeV is presented. The K^{*}(892)[±] resonance signal is reconstructed via the invariant mass method from the decay channel K^{*}(892)[±] → K_S⁰π[±] where K_S⁰, in turn, is obtained from its decay to a pair of oppositely charged pions, K_S⁰ → π⁺π[−]. As the quark content of K^{*}(892)[±] (us> and us>) is similar to that of K^{*}(892)⁰ (ds> and ds>), their momentum distributions are expected to be comparable with each other. Their masses differ by about (0.0067 ± 0.0012) GeV/c² ($M_{\text{K}^*(892)^0} = (0.8955 \pm 0.0002)$ GeV/c² and $M_{\text{K}^*(892)^{\pm}} = (0.8916 \pm 0.0002)$ GeV/c²), and their lifetimes by about 0.16 fm/c ($\tau_{\text{K}^*(892)^0} \approx 4.16$ fm/c and $\tau_{\text{K}^*(892)^{\pm}} \approx 4$ fm/c). Thus, this measurement will complement and verify the experimental findings for K^{*}(892)⁰ [39] by using the particle reconstruction techniques characterized by different systematic uncertainties. The measurement will also complete the first excited state measurements of the kaon family. The system size dependence of p_{T} -integrated and p_{T} -differential particle yield ratios $2\text{K}^*(892)^{\pm}/(\text{K}^+ + \text{K}^-)$ are presented along with model comparisons to shed light on the rescattering and regeneration effects in the hadronic phase. The variation of hadronic phase lifetime with collision centrality is studied by extracting the kinetic freeze-out temperature using the HRG-PCE model [59] assuming a constant chemical freeze-out temperature as a function of centrality. The flavor dependence of R_{AA} is tested further with the inclusion of K^{*}(892)[±] meson along with other light-flavored hadrons.

Throughout this article, the results for K^{*}(892)⁺, K^{*}(892)[−] and K^{*}(892)⁰, $\overline{\text{K}^*}(892)^0$ are averaged and denoted as K^{*±} and K^{*0}, respectively, unless otherwise stated. Also, K and π in this article refer to the average of particle and antiparticle yields, (K⁺ + K[−])/2 and (π⁺ + π[−])/2, respectively. The article is organized as follows. Section 2 describes the ALICE experimental setup. In Section 3, the data analysis technique, including the event and track selection criteria applied, yield extraction procedure, and systematic uncertainties are described. Section 4 presents the results related to the K^{*±} meson. Finally, the article is concluded with a summary in Section 5.

2 Experimental apparatus

The production yield of the K^{*±} mesons is measured in Pb–Pb collisions at $\sqrt{s_{\text{NN}}} = 5.02$ TeV using the data collected by the ALICE detector in the year 2018. A complete description of the ALICE detector can be found in Refs. [60, 61]. This analysis is performed by using the information from the Inner Tracking System (ITS) [62], Time Projection Chamber (TPC) [63], Time-of-Flight (TOF) [64, 65] and V0 [66] detectors.

The ITS and TPC detectors are located inside a large solenoidal magnet with a magnetic field strength

of 0.5 T. They are used for charged-particle tracking, reconstruction of the primary vertex and particle identification. The ITS, TPC, and TOF detectors span the full azimuthal coverage, covering a pseudo-rapidity range of $|\eta| < 0.9$. The ITS detector consists of six cylindrical layers of silicon detectors and is the innermost ALICE detector surrounding the beam pipe. The layer radii vary between 3.9 and 43 cm. The ITS is used for precise reconstruction of the event primary vertex (PV) and improvement of the angular and momentum resolution of tracks reconstructed in the TPC. The TPC is the main ALICE detector for tracking and identification of charged particles. It provides three-dimensional space point information for charged particles. The maximum number of crossed pad rows for a full-length reconstructed track is 159 in the TPC. Particle identification (PID) in the gas-filled TPC is achieved by the specific energy loss (dE/dx) measured for reconstructed charged-particle tracks. The dE/dx resolution of the TPC detector is around 5% for tracks with 159 clusters, and when averaged over all tracks, it is about 6.5%. The TPC detector provides greater than 2σ separation between pions and kaons in $0.2 < p_T < 0.7$ GeV/c and between kaons and protons in $0.4 < p_T < 0.8$ GeV/c [56]. The TOF is a gaseous detector, built of Multigap Resistive Plate Chambers (MRPC) with a time resolution of 80 ps. The TOF detector provides a 2σ separation between pions and kaons at $p_T < 3.2$ GeV/c and between kaons and protons at $p_T < 5.4$ GeV/c [56].

Two scintillator detectors, V0A ($2.8 < \eta < 5.1$) and V0C ($-3.7 < \eta < -1.7$), which are located on either side of the interaction point along the beam line and have a time resolution of less than 1 ns, are used for event triggering and beam induced background rejection. The measured V0M (V0A + V0C) signal is proportional to the total charge accumulated in the detectors [66] and is used to classify Pb–Pb events into different centrality classes. A Glauber Monte Carlo model [55] is fitted to the measured V0M amplitude distribution to compute the fraction of hadronic cross section sampled by the trigger.

3 Data analysis

The yield of the K^{*±} meson is reconstructed via its hadronic decay channel, $K^{*\pm} \rightarrow K_S^0 \pi^\pm$, with BR = $(33 \pm 0.003)\%$ [67] at midrapidity $|y| < 0.5$, taking into consideration the decay channel $K^{*\pm} \rightarrow K^0 \pi^\pm$ and a probability of 0.5 for K^0 be K_S^0 . The analysis is performed in five different centrality intervals, 0–10%, 10–20%, 20–40%, 40–60% and 60–80%, in the transverse momentum range from 0.4 GeV/c to 16 GeV/c. The K_S^0 is reconstructed by exploiting its weak decay topology (V⁰ topology) into two oppositely charged particles ($K_S^0 \rightarrow \pi^- \pi^+$) with a branching ratio of $(69.2 \pm 0.05)\%$ [67].

3.1 Event and Track selections

The analyzed data, which correspond to an integrated luminosity of $20 \mu\text{b}^{-1}$ were collected in 2018 using a minimum bias (MB) trigger that requires a coincidence of signals in both the V0A and V0C detectors. Only events with the reconstructed event vertex lying within 10 cm from the nominal interaction point are accepted in the analysis. The events containing more than one reconstructed vertex are tagged as pile-up events in the same bunch crossing and discarded from the analysis. After all the event selection criteria, the total number of analyzed events is $\approx 1.2 \times 10^8$. Charged pions from $K^{*\pm} \rightarrow K_S^0 \pi^\pm$ decays are reconstructed as primary tracks using signals measured both in the ITS and TPC detectors. Charged pions from weak decays ($K_S^0 \rightarrow \pi^- \pi^+$) are reconstructed as secondary tracks using the TPC only. For high tracking efficiency, a minimum requirement of 70 out of the maximum possible 159 TPC hits are required for primary and secondary tracks. The χ^2 of the reconstructed tracks, which quantifies the deviation between the measured hits and the expected positions of the tracks in the TPC and ITS detectors, normalized to the number of measured hits in each detector is required to be less than 4 and 36, respectively. These thresholds ensure that the reconstructed tracks closely match the expected positions within a reasonable range of uncertainty. The primary tracks are required to have a distance of closest approach to the primary vertex, $DCA_{xy} < 7\sigma$, where $\sigma = 0.0105 + (0.0350/p_T^{1.1})$ in the transverse plane and within $|DCA_z| < 2$ cm along the beam direction. Only tracks with transverse momentum $p_T > 0.15$

GeV/ c and pseudorapidity $|\eta| < 0.8$ are accepted for the analysis. The PID for primary charged-particle tracks is achieved by requiring the specific energy loss (dE/dx) in the TPC gas to be consistent with the signal expected for a charged pion within two standard deviations $2\sigma_{\text{TPC}}$. If the track is matched with a signal in the TOF, it is additionally required that the measured time of flight is consistent with that expected for a charged pion within $3\sigma_{\text{TOF}}$ [63, 68].

The secondary particle, K_S^0 , is reconstructed based on weak decay topological criteria [69]. Selection criteria for K_S^0 reconstruction are listed in Table 1. Two oppositely charged tracks lying in the acceptance window $|\eta| < 0.8$ are identified as pions (daughters of K_S^0) based on a $4\sigma_{\text{TPC}}$ selection criterion. The DCA between negatively and positively charged tracks is required to be smaller than 0.8 cm. Furthermore, the DCA of charged tracks to the primary vertex is required to be greater than 0.1 cm. Also, a requirement of less than 0.3 cm on the DCA of the V^0 particle to the primary vertex in the transverse plane is applied. The cosine of the pointing angle, which refers to the angle between the V^0 momentum and the line connecting the secondary to the primary vertex, is required to be greater than 0.98. Only those V^0 candidates with a radius of the reconstructed secondary vertex larger than 1.6 cm are chosen. Furthermore, K_S^0 candidates exhibiting a proper lifetime, calculated as LM_{K^0S}/p , where L represents the linear distance between the primary and secondary vertex, M_{K^0S} denotes the mass of K_S^0 , and p indicates the total momentum of K_S^0 , exceeding 15 cm are eliminated to mitigate the presence of combinatorial background arising from interactions with the detector material. To improve the signal-to-background ratio under the K_S^0 peak, a selection criterion is imposed on the asymmetry of pion momenta (Armenteros parameter), $(p_{\pi^-} - p_{\pi^+})/(p_{\pi^-} + p_{\pi^+})$, allowing only pairs of pions with an Armenteros parameter value exceeding 0.2 to be considered. Finally, the invariant mass of $\pi^+\pi^-$ is required to be compatible within 2σ of the K_S^0 nominal mass, where σ is the detector mass resolution, which is found to be equal to ≈ 5 MeV/ c^2 with a very weak dependence on collision centrality and particle momentum. After all these topological criteria, only those K_S^0 candidates with $|y| < 0.5$ are analyzed.

Table 1: Selection criteria for K_S^0 .

Selection criteria	Value	Variations
Crossed rows	> 70	60, 80
Acceptance window of pions ($ \eta $)	< 0.8	-
Pion dE/dx (σ)	< 4	3, 5
DCA V^0 daughters	< 0.8 cm	0.4, 0.5 cm
DCA of V^0 daughters to PV	> 0.1 cm	-
DCA of V^0 particle to PV	< 0.3 cm	0.4, 0.5 cm
V^0 cosine pointing angle	> 0.98	0.985, 0.995
V^0 radius	> 1.6 cm	1 cm
Proper lifetime	< 15 cm	12, 20 cm
Armenteros parameter	> 0.2	-
K_S^0 mass window (σ)	± 2	-

3.2 Yield extraction

The reconstructed K_S^0 and π^\pm candidates are paired in the same events. Only pairs in the rapidity range $|y| < 0.5$ are selected. The invariant mass distribution of $K_S^0\pi^\pm$ consists of a signal peak hidden under a large combinatorial background. The combinatorial background from uncorrelated $K_S^0\pi^\pm$ pairs is estimated using a mixed-event technique. The mixed-event invariant mass distribution is accumulated by pairing K_S^0 from one event with π^\pm from different events. The mixed events are required to belong to the same centrality intervals, and the absolute difference between the primary vertex positions in the beam direction is required to be less than 1 cm. Each event is mixed with ten other events to reduce the statistical fluctuations in the mixed-event invariant mass distributions. The selected number of mixed events led to minimal additional statistical uncertainties in the results following the subtraction of the

mixed-event background. This approach ensured that computational efficiency was maintained at an acceptable level. The $K_S^0\pi^\pm$ invariant mass distribution obtained from the mixed events is normalized in the range of masses 1.2–1.3 GeV/c^2 to have the same integral as for the same event $K_S^0\pi^\pm$ invariant mass distribution. After the subtraction of the normalized mixed-event combinatorial background from the same event $K_S^0\pi^\pm$ distribution, the signal peak is observed on top of a residual background. The sources of this residual background are the correlated $K_S^0\pi^\pm$ pairs emitted within a jet, correlated pairs from decaying particles, and correlated pairs from misidentified decays. Invariant mass distributions for $K_S^0\pi^\pm$ pairs were obtained in the Monte Carlo analysis using the same event and track selections as in data. The study showed that the correlated background has a smooth dependence on the mass. The left panel of Fig. 1 shows an example of the invariant mass distribution of $K_S^0\pi^\pm$ pairs from the same events and the normalized mixed event background distribution for the transverse momentum range $2.5 < p_T < 3.0 \text{ GeV}/c$ for 0–10% Pb–Pb collisions. The right panel of the same figure shows the invariant mass distribution after the mixed-event background subtraction. The subtracted invariant mass distribution is fitted using a combined function to describe both the signal peak, and residual background. For the signal peak, a Breit–Wigner function is used, and for the residual background, a product of an exponential function and a polynomial of second order is used.

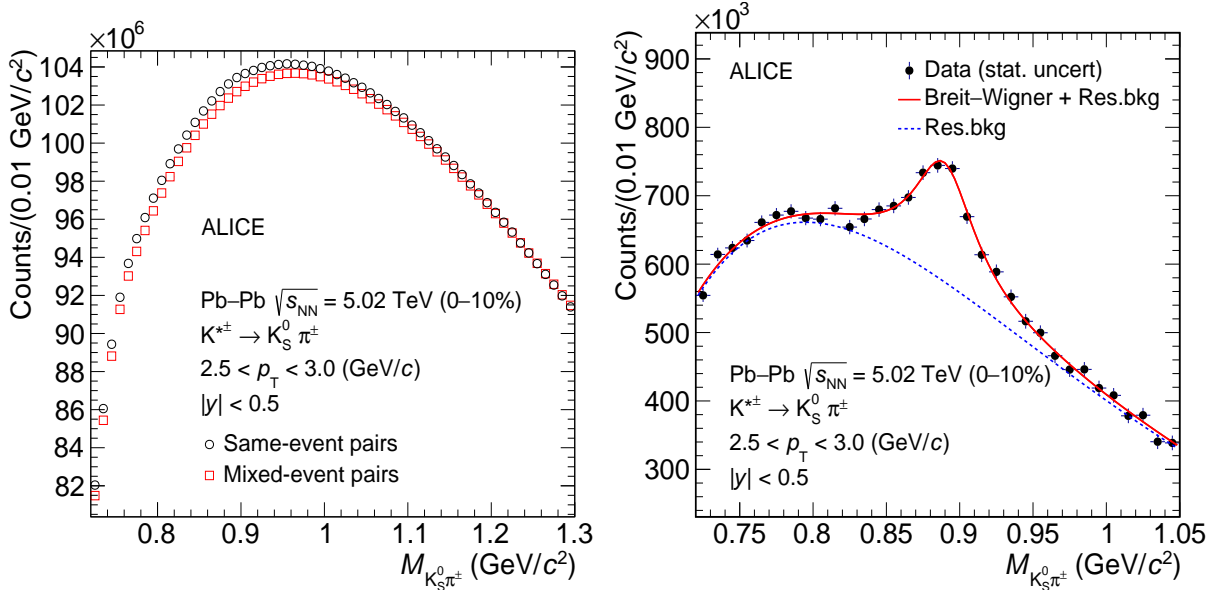


Figure 1: (Left panel): Invariant mass distribution of $K_S^0\pi^\pm$ pairs in same (black marker) and mixed events (red marker). (Right panel): Invariant mass distribution of $K_S^0\pi^\pm$ pairs after the subtraction of normalized mixed-event background distribution. The solid red curve is the fit function defined by Eq. 2, with the dotted blue line describing the residual background distribution given by Eq. 3

The fit function is defined as

$$\frac{dN}{dM} = \frac{Y}{2\pi} \frac{\Gamma_0}{(M - M_0)^2 + \Gamma_0^2/4} + \text{Res.bkg}, \quad (2)$$

where M_0 and Γ_0 are the mass and width of $K^{*\pm}$, M is invariant mass of the $K_S^0\pi^\pm$ pair ($M_{K_S^0\pi^\pm}$), and the parameter Y is the normalization constant. The mass resolution of the detector for reconstruction of $K^{*\pm}$ is negligible as compared with the vacuum width of the $K^{*\pm}$ (0.0514 ± 0.0009) GeV/c^2 [67], hence it is not included. The last term in Eq. 2 is a residual background function (Res.bkg) taken as

$$\text{Res.bkg} = [M - (m_{\pi^\pm} + M_{K_S^0})]^n \exp(A + BM + CM^2), \quad (3)$$

where m_{π^\pm} and $M_{K_S^0}$ are the mass of the pion, and K_S^0 , respectively, and A, B, C, and n are the fit parameters. This form of residual background is motivated from Ref. [69]. During fitting, by default, the Γ_0 parameter was set equal to the vacuum width of the $K^{*\pm}$ meson. The raw particle yields are then obtained by integrating the invariant mass distribution within the mass interval $M_0 \pm 2\Gamma_0$ and subtracting from it the integral of the residual background function in the same mass region. The yield of the resonance in the peak tails beyond the counting range is obtained by integrating the tail part of the signal fit function in the corresponding mass ranges. The tail part contributes $\approx 13\%$ of the total yield, and the fraction does not depend on p_T or collision centrality. The significance of the $K^{*\pm}$ peak presented in Fig. 1 is 23.

3.3 Efficiency and acceptance

The measured yields are corrected for the detector acceptance and reconstruction efficiency ($A \times \epsilon_{\text{rec}}$), which were evaluated using a detailed Monte Carlo simulation of the ALICE detector. The Pb–Pb collisions at $\sqrt{s_{\text{NN}}} = 5.02$ TeV were generated using the HIJING event generator [70]. The produced particles were traced through detector materials using GEANT3 simulations [71]. The $A \times \epsilon_{\text{rec}}$, defined as the ratio of reconstructed to generated $K^{*\pm}$, was calculated as a function of p_T within $|y| < 0.5$. Only those $K^{*\pm}$ that decay into $K^0\pi^\pm$ channel, taking into account the 0.5 probability of K^0 to be K_S^0 , were accounted in the denominator. The same track and PID selections used in data were considered in the simulation as well. Since the reconstruction efficiency depends on the shape of the generated $K^{*\pm}$ meson p_T spectra, they were reweighted to reproduce the measured ones. The reweighting procedure required several iterations to converge. The reweighting resulted in the reduction of $A \times \epsilon_{\text{rec}}$ by $\approx 4\text{--}6\%$ at low momentum, $p_T < 1$ GeV/c, and negligible corrections at higher momenta.

The evaluated detector acceptance and reconstruction efficiencies for different centrality intervals are shown in Fig. 2. For each centrality interval, $A \times \epsilon_{\text{rec}}$ rises at low p_T , reaches the maximum at $p_T \approx 4$ GeV/c and then decreases at higher momenta. This decrease in the efficiency at higher momenta is due to the reduced probability of K_S^0 reconstruction with the selection criteria described in the previous section. The efficiencies show a strong centrality dependence with a maximum magnitude varying from 0.15 to 0.21 in 0–10% to 60–80% centrality intervals, respectively.

The p_T -differential raw yields of $K^{*\pm}$ are finally corrected using the $A \times \epsilon_{\text{rec}}$ of the respective centrality intervals. The corrected yields are given by

$$\frac{1}{N_{\text{event}}} \frac{d^2N}{dydp_T} = \frac{1}{N_{\text{event}}^{\text{acc}}} \frac{d^2N^{\text{raw}}}{dydp_T} \frac{1}{(A \times \epsilon_{\text{rec}})\text{BR}}, \quad (4)$$

where dy, dp_T are the widths of the analyzed rapidity and p_T intervals, respectively. As seen from the above equation, the raw yields are normalized to the number of accepted events in the centrality interval ($N_{\text{event}}^{\text{acc}}$) and branching ratio (BR) of the decay channel.

3.4 Systematic uncertainties

The systematic uncertainties in the measurement of $K^{*\pm}$ yields are summarized in Table 2. The total systematic uncertainty includes contributions from the signal extraction method, primary and secondary track selection criteria, PID, global tracking efficiency, knowledge of the ALICE material budget, and interaction cross section of hadrons with the detector material. The total uncertainty is calculated by summing the uncertainties from each source in quadrature. The uncertainties are found to be similar in various measured centrality intervals. The uncertainty values given in the table are reported for three p_T intervals averaged over all measured centralities.

The uncertainty in the signal extraction is assessed by varying several factors, including fitting ranges, mixed-event background normalization ranges, residual background fit functions, and yield extraction methods. Additionally, the default fits to the invariant mass distributions are repeated with the width

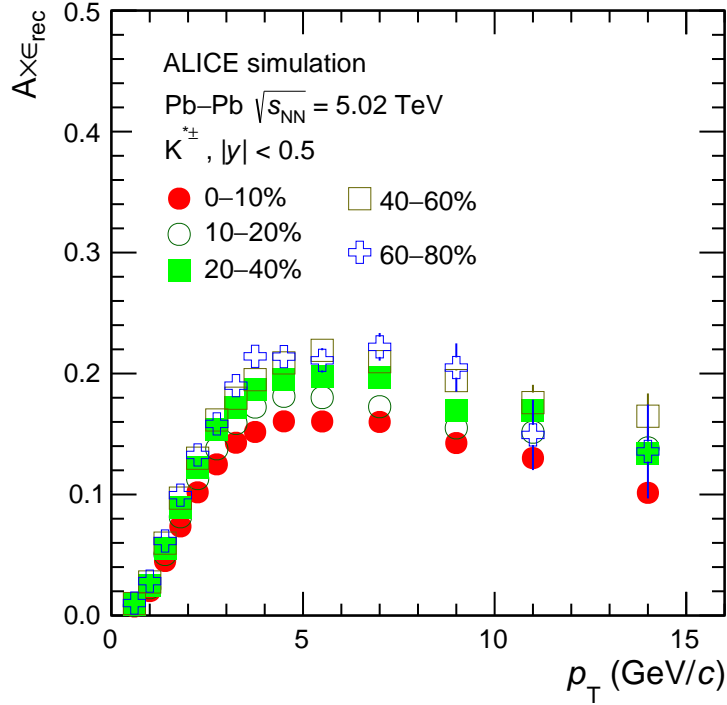


Figure 2: The acceptance times efficiency correction for $K^{*\pm}$ as a function of transverse momentum for different centrality intervals.

Table 2: Systematic uncertainties for $K^{*\pm}$ in Pb–Pb collisions at $\sqrt{s_{\text{NN}}} = 5.02$ TeV. The systematic uncertainties are shown for low, intermediate, and high p_T intervals averaged over all centralities.

Systematic variation	Low p_T (GeV/c) 0.4–0.8	Mid p_T (GeV/c) 2.0–2.5	High p_T (GeV/c) 12.0–16.0
Signal extraction (%)	7.4	5.2	5.6
Primary track selection (%)	5	3.3	4.7
K_S^0 reconstruction (%)	5.4	3.8	4.6
PID (%)	3.7	2.3	3.2
Global tracking efficiency (%)	3	3.9	2.2
Material budget (%)	3.1	1.1	0.5
Hadronic interaction (%)	1	0.9	negl.
Total (%)	12	8.8	9.6

of $K^{*\pm}$ treated as a free parameter. The choice of fitting range in the default case is determined based on the background shape. As part of the systematic uncertainty evaluation, the boundaries of the fitting ranges are adjusted by 20 MeV/ c^2 on both sides. The mixed-event normalization range is shifted from the default range of 1.2–1.3 GeV/ c^2 to 1.1–1.2 GeV/ c^2 and 1.3–1.4 GeV/ c^2 . To study systematic effects, the residual background is modeled using second- and third-order polynomials. The resultant uncertainty for signal extraction from different sources is determined as the RMS of the particle yields obtained with different variations and ranges from 5.2% to 7.5%. For primary track selection, the criteria are varied following the procedure described in Ref. [39] to investigate the systematic impact of track selections. The resulting uncertainty varies from 3.3% to 5%. By varying the topological selection criteria provided in Table 1, the uncertainty in K_S^0 reconstruction is found to be in the range of 3.7% to 5.8%. To determine the yield uncertainty associated with the identification of primary daughter tracks, the selection criteria in the TPC ($1.5 < |\eta|_{\text{TPC}} < 3.0$) and TOF ($3 < |\eta|_{\text{TOF}} < 4.0$) are varied. The resulting uncertainty ranges from 1.7% to 3.9%. The global tracking uncertainty, originating from efficiency of the ITS–TPC

track matching, is determined based on the single-particle tracking uncertainty of charged particles [56], reaching a maximum of approximately 4%. Uncertainties related to the material budget and hadronic cross section, as obtained from Ref. [69], contribute up to 3% and 1% respectively. Taking all these factors into account, the average total uncertainty ranges from 8.8% to 12%. The total uncertainty for K^{*±} is found to be similar to that of K^{*0} [39]. Among the systematic uncertainties, only the signal extraction uncertainty is a fully uncorrelated source, while track selection, PID, global tracking efficiency, material budget, and hadronic interaction are correlated across different centrality intervals.

4 Results and discussions

4.1 Transverse momentum spectra

The fully corrected p_{T} distributions for K^{*±} meson at midrapidity for centrality intervals 0–10%, 10–20%, 20–40%, 40–60%, and 60–80% are shown in Fig. 3. The transverse momentum spectra become harder from peripheral to central collisions.

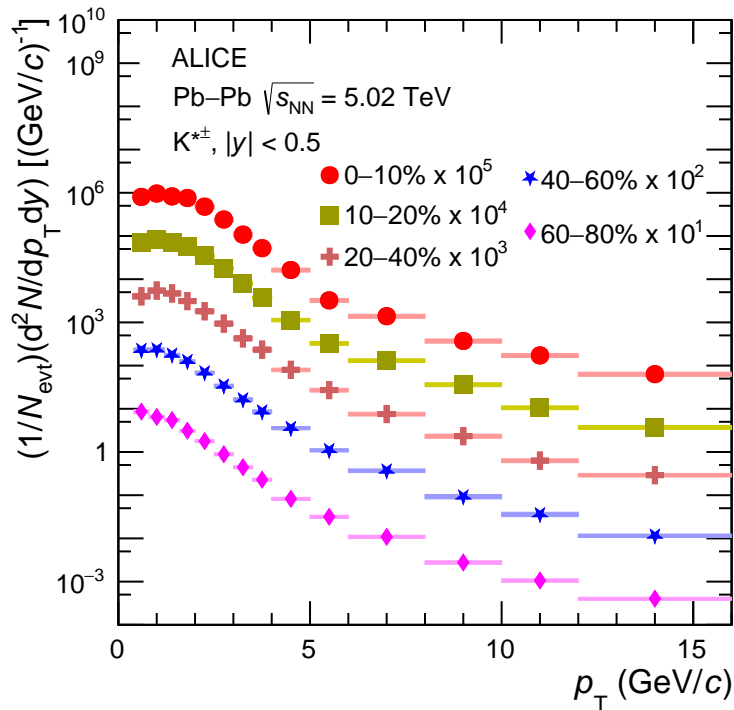


Figure 3: The p_{T} distributions of K^{*±} meson in various centrality intervals in Pb–Pb collisions at $\sqrt{s_{\text{NN}}} = 5.02$ TeV. The statistical and systematic uncertainties are shown as bars and boxes, respectively.

Figure 4 compares the transverse momentum distributions of K^{*±} and K^{*0} mesons in Pb–Pb collisions at $\sqrt{s_{\text{NN}}} = 5.02$ TeV for the 0–10% and 40–60% centrality intervals. The bottom panels of Fig. 4 show the ratio of K^{*±} to K^{*0}. The statistical and systematic uncertainties on the ratio are obtained by propagating the corresponding statistical and total systematic uncertainties on the K^{*0} and K^{*±} p_{T} spectra. The ratio is consistent with unity within uncertainties. A similar consistency of the spectra for K^{*±} and K^{*0} has been previously observed in pp collisions [69].

4.2 dN/dy and $\langle p_{\text{T}} \rangle$

To extract the p_{T} -integrated particle yield (dN/dy) and average transverse momentum ($\langle p_{\text{T}} \rangle$) for each centrality interval, the measured p_{T} distributions of K^{*±} are integrated, while fit functions are used to estimate the resonance yield in the unmeasured p_{T} regions. The fully corrected p_{T} distributions are fitted

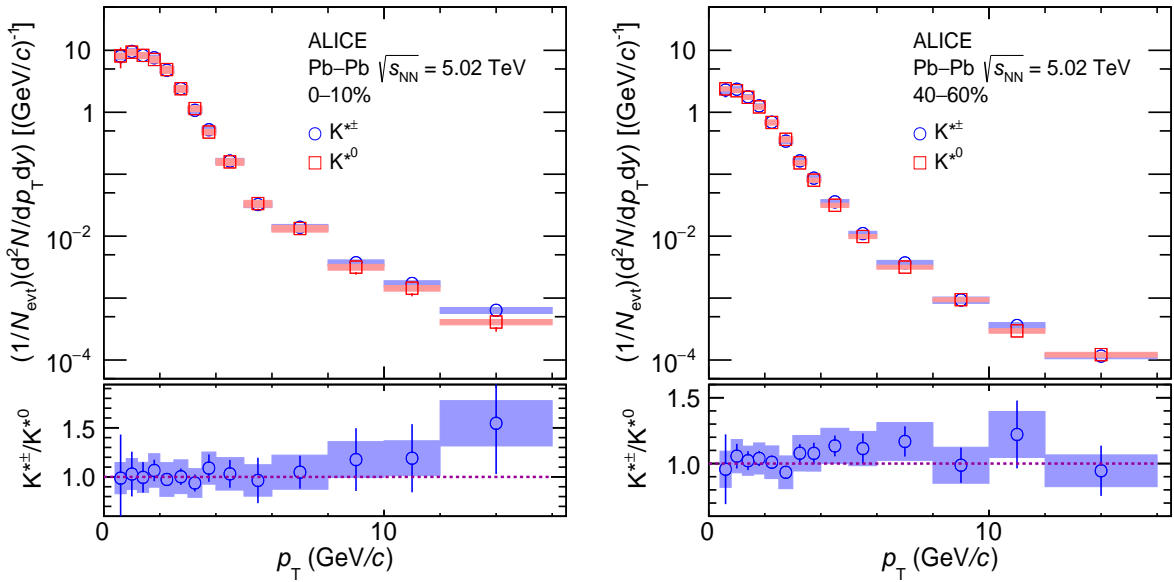


Figure 4: The p_T distributions of $K^{*\pm}$ (blue circles) and K^{*0} (red squares) [39] in 0–10% (left) and 40–60% (right) centrality intervals in Pb–Pb collisions at $\sqrt{s_{\text{NN}}} = 5.02$ TeV. Statistical and systematic uncertainties are shown by bars and shaded boxes, respectively. The bottom panels show the $K^{*\pm}$ to K^{*0} ratio as a function of p_T .

with Boltzmann–Gibbs blast-wave function [72] in the p_T range 0.4–3.5 GeV/ c . The fit function is then extrapolated down to zero transverse momentum. The low p_T extrapolation (< 0.4 GeV/ c) accounts for 8% (12%) of the total yield in the 0–10% (60–80%) centrality interval. Various fitting functions, including Levy–Tsallis, Boltzmann–Gibbs, and Bose–Einstein [73, 74], are employed to assess their impact on the integrated dN/dy and $\langle p_T \rangle$. The variations in dN/dy and $\langle p_T \rangle$ due to the choice of different fitting functions are incorporated into the systematic uncertainties. The left panel of Fig. 5 shows dN/dy of $K^{*\pm}$ measured at midrapidity ($|y| < 0.5$) as a function of average charged-particle pseudorapidity density ($\langle dN_{\text{ch}}/d\eta \rangle_{|\eta| < 0.5}$) in Pb–Pb collisions at $\sqrt{s_{\text{NN}}} = 5.02$ TeV. The results for K^{*0} in Pb–Pb collisions at $\sqrt{s_{\text{NN}}} = 5.02$ TeV and $\sqrt{s_{\text{NN}}} = 2.76$ TeV are also shown for comparison. For a given charged-particle multiplicity, the dN/dy of $K^{*\pm}$ is consistent with the K^{*0} measurements at 2.76 TeV and 5.02 TeV. This signifies that resonance production is purely driven by charged-particle multiplicity and not by collision energy at the LHC. The right panel of Fig. 5 shows the $\langle p_T \rangle$ of $K^{*\pm}$ at $\sqrt{s_{\text{NN}}} = 5.02$ TeV together with K^{*0} measurements at $\sqrt{s_{\text{NN}}} = 5.02$ TeV and 2.76 TeV. The $\langle p_T \rangle$ values increase with increasing charged-particle multiplicity, which is consistent with the picture of a growing contribution of radial flow with $\langle dN_{\text{ch}}/d\eta \rangle_{|\eta| < 0.5}$ [56]. The central values of $\langle p_T \rangle$ for $K^{*\pm}$ and K^{*0} at $\sqrt{s_{\text{NN}}} = 5.02$ TeV are systematically higher than at $\sqrt{s_{\text{NN}}} = 2.76$ TeV, although consistent within systematic uncertainties, which are rather large in the latter case. The results are compared with MUSIC with and without SMASH afterburner model predictions [75, 76]. MUSIC is a hydrodynamic-based model with SMASH as an afterburner on top of the hydrodynamic expansion to simulate the hadronic interactions. In this model, the probability of resonance disappearing is proportional to the Knudsen number $\text{Kn} = \lambda/L$, where λ is the mean free path of the resonance and L is the system size. The model does not take into account the regeneration of resonances. Rapid kinetic freeze-out simultaneously for all species is assumed, and the centrality dependence of resonance suppression originates from different temperatures of kinetic freeze-out for different centrality intervals. MUSIC and MUSIC+SMASH results are only shown for K^{*0} in Pb–Pb collisions at $\sqrt{s_{\text{NN}}} = 5.02$ TeV as no significant quantitative difference between predictions for K^{*0} and $K^{*\pm}$ is expected. MUSIC and MUSIC+SMASH both overpredict the yield measurements and underpredict the $\langle p_T \rangle$ of the $K^{*\pm}$. MUSIC+SMASH is closer to the measurements than MUSIC only predictions.

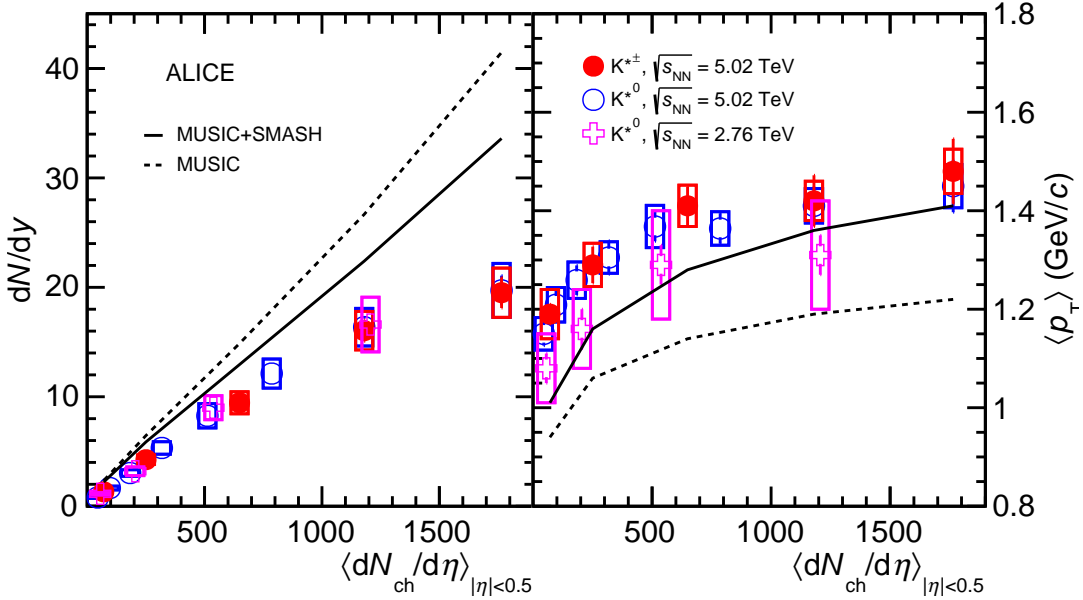


Figure 5: The dN/dy (left) and $\langle p_T \rangle$ (right) as a function of system size for $K^{*\pm}$ (closed marker) and K^*0 (open markers) [39] in Pb–Pb collisions at $\sqrt{s_{\text{NN}}} = 5.02 \text{ TeV}$ and $\sqrt{s_{\text{NN}}} = 2.76 \text{ TeV}$ [77]. Comparison with predictions of MUSIC hydrodynamic model with and without the hadronic phase afterburner (SMASH) are presented by solid and dashed lines, respectively. Statistical (systematic) uncertainties are shown by bars (boxes).

4.3 Freeze out temperature using the HRG-PCE model

The thermodynamic properties of the system created in heavy-ion collisions can be studied using thermal model calculations. In this study, the hadron resonance gas (HRG) model in partial chemical equilibrium (PCE) [59] is used to extract the freeze-out parameters of the system. The evolution of the system in partial chemical equilibrium follows the conservation of the total yields and entropy of the stable hadrons. Resonance decays and formation take place, obeying the law of mass action. Including resonances in the HRG-PCE model fit is necessary for the PCE evolution of the system in the hadronic phase. The model parameters are the baryon chemical potential (μ_B), the chemical freeze-out temperature (T_{ch}), the kinetic freeze-out temperature (T_{kin}), the volume (V_{ch}) of the system formed at freeze-out and the fugacity parameters which regulate deviations from chemical equilibrium in the light and strange quark sectors. It is assumed that $\mu_B = 0$, and yields of particles and antiparticles are the same. The chemical freeze-out temperature is fixed to 155 MeV, and all fugacity parameters to unity. The free parameters of the fit are the kinetic freeze-out temperature, and the volume. The kinetic freeze-out temperature is extracted from the HRG-PCE model [59] fit to the yields of π , K , p , ϕ , K^*0 and $K^{*\pm}$ in Pb–Pb collisions at $\sqrt{s_{\text{NN}}} = 5.02 \text{ TeV}$. The procedure for fitting the HRG-PCE model to the data is implemented in THERMAL-FIST [78] since version 1.3. The temperature is determined for five different centrality intervals 0–10%, 10–20%, 20–40%, 40–60%, and 60–80% as shown in Table 3 and compared with the results of blast-wave fits to the p_T spectra of π^\pm , K^\pm , $p(\bar{p})$ [56]. The fitting of p_T spectra depends on the assumed flow velocity profile and the freeze-out hypersurface within the blast-wave model. The concept of the HRG-PCE model is free from these assumptions. Table 3 shows that results from the HRG-PCE model are consistent within uncertainties with the published blast-wave model results.

The extracted kinetic freeze-out temperature increases from 95 MeV in 0–10% Pb–Pb collisions to 124 MeV in 60–80% Pb–Pb collisions. The results indicate the presence of the hadronic phase of a finite lifetime in heavy-ion collisions, longer lived in central collision and shorter in peripheral collision.

Table 3: HRG-PCE model fits results in Pb–Pb collisions at $\sqrt{s_{\text{NN}}} = 5.02 \text{ TeV}$. Numbers in brackets show the published kinetic freeze-out temperatures obtained using blast-wave fits to π^{\pm} , K^{\pm} , $p(\bar{p})$ spectra [56].

Centrality (%)	$T_{\text{kin}} (\text{MeV})$	χ^2/Ndf
0–10	95 ± 3 (91 ± 3)	2.25
10–20	104 ± 4 (94 ± 3)	2.17
20–40	109 ± 5 (99 ± 3)	1.48
40–60	116 ± 6 (112 ± 3)	0.77
60–80	124 ± 8 (138 ± 6)	1.63

4.4 Particle ratios

Ratios of resonance yields to those of longer-lived particles with similar quark contents are constructed to numerically study the effects of rescattering and regeneration processes. Figure 6 shows the p_{T} -integrated yield ratios of $K^{*\pm}/K$, K^{*0}/K and ϕ/K as a function of $\langle dN_{\text{ch}}/d\eta \rangle_{|\eta|<0.5}^{1/3}$ in Pb–Pb collisions at $\sqrt{s_{\text{NN}}} = 5.02 \text{ TeV}$ and $K^{*\pm}/K$ in pp collisions at $\sqrt{s} = 5.02 \text{ TeV}$ [39, 56, 69]. The $\langle dN_{\text{ch}}/d\eta \rangle_{|\eta|<0.5}^{1/3}$ is proportional to the linear (radial) path through the produced matter. The kaon yields in Pb–Pb collisions at $\sqrt{s_{\text{NN}}} = 5.02 \text{ TeV}$ are taken from Ref. [56].

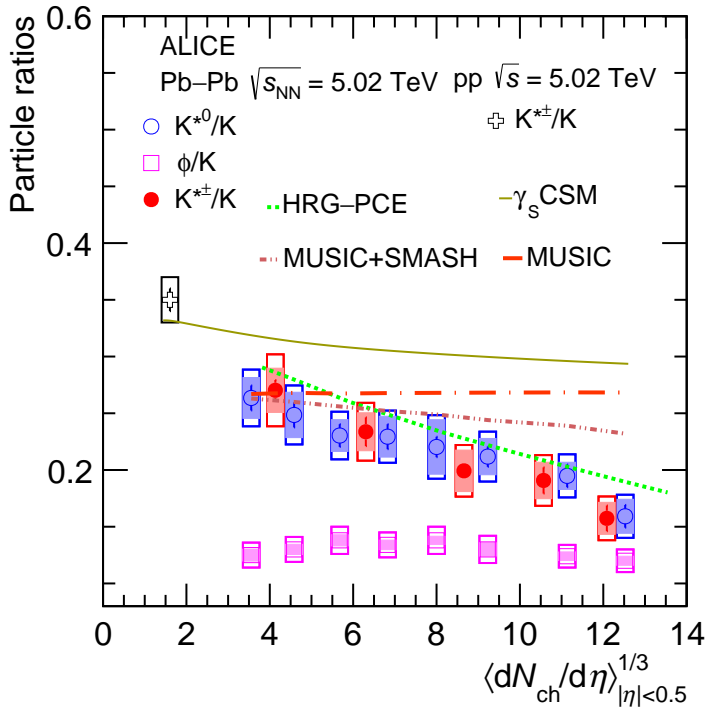


Figure 6: The p_{T} -integrated particle yield ratios $K^{*\pm}/K$, K^{*0}/K and ϕ/K measured at midrapidity ($|y| < 0.5$) in pp and Pb–Pb collisions at $\sqrt{s_{\text{NN}}} = 5.02 \text{ TeV}$ as a function of $\langle dN_{\text{ch}}/d\eta \rangle_{|\eta|<0.5}^{1/3}$. For Pb–Pb collisions, K^{*0}/K and ϕ/K data points are taken from Ref. [39] and for pp collisions $K^{*\pm}/K$ is taken from Ref. [69]. The results of the Gamma canonical statistical model calculation [79] for K^{*0}/K , in addition to predictions from the HRG-PCE model [59], as well as MUSIC with and without afterburner [75] are shown. Statistical uncertainties are shown by bars, total systematic uncertainties by open boxes, and the multiplicity-uncorrelated systematic uncertainty by the shaded boxes. The two highest multiplicity data points for K^{*0} and ϕ mesons are slightly shifted for visibility.

The p_{T} -integrated $K^{*\pm}/K$ ratio decreases with increasing system size. The suppression of the $K^{*\pm}/K$ ratio is similar to that of K^{*0}/K at similar multiplicity. This is consistent with the picture of the rescattering effect for the decay products in the hadronic phase. The lifetime of the ϕ meson is one order of magnitude longer than that of the K^* meson, hence its decay products are not expected to take part in rescattering

processes, while the regeneration of kaons can increase the measured ϕ meson yields. A constant ϕ/K ratio as a function of charged-particle multiplicity indicates that neither rescattering nor regeneration plays an important role for the ϕ meson in the hadronic medium.

For comparison, the predictions of the Gamma canonical statistical model (γ_S CSM) [79], HRG-PCE [59], hydrodynamic model MUSIC with and without hadronic afterburner [75] for K^{*}⁰/K are also shown in Fig.6. Generally, the statistical models involve an ideal hadron resonance gas in thermal and chemical equilibrium at the chemical freeze-out surface. The baryon number, the strangeness, and the electric charges are fixed to a particular value and remain conserved exactly across the correlation volume V_c . In the Gamma canonical statistical model, a multiplicity-dependent chemical freeze-out temperature is considered, where the possibility of incomplete chemical equilibrium in the strangeness sector is included via the γ_S factor. The canonical volume considered in this model corresponds to three units of rapidity $V_c = 3 \text{ dV/dy}$. The model overpredicts the measurements and predicts a relatively flat ratio with increasing system size. The prediction from MUSIC with SMASH as an afterburner also fails to describe the level of suppression as observed in the experimental data. The hadron resonance gas model in partial chemical equilibrium, which incorporates the hadronic phase, qualitatively describes the experimental data. This suggests the importance of the rescattering effect for the measured K^{*}[±] yields in the hadronic phase of heavy-ion collisions.

The significance of the suppression of the yield ratio (K^{*}[±]/K) in central Pb–Pb collisions with respect to pp collisions can be quantified using the double ratio (K^{*}[±]/K)_{PbPb}/(K^{*}[±]/K)_{pp} = 0.448 ± 0.057, where the multiplicity uncorrelated uncertainty for K^{*}[±] and total uncertainty for K are considered. This double ratio deviates from unity by 9.3 standard deviations. The suppression of the K^{*}[±]/K ratio is found to be similar to that of K^{*}⁰/K, but measured with higher precision (9.3 σ compared with 6.02 σ) [39].

The p_T -differential yield ratios are measured in order to study the p_T dependence of the rescattering effect. The upper panels of Fig.7 show the p_T -differential yield ratios of K^{*}[±]/K (a) and K^{*}[±]/ π (b) in Pb–Pb collisions at $\sqrt{s_{\text{NN}}} = 5.02 \text{ TeV}$ for 0–10%, 60–80% centrality intervals compared with pp collisions at $\sqrt{s_{\text{NN}}} = 5.02 \text{ TeV}$ [69]. The bottom panels (c and d) show the double ratios. At low p_T (< 2 GeV/c), the double ratios (K^{*}[±]/K)_{PbPb}/(K^{*}[±]/K)_{pp} and (K^{*}[±]/ π)_{PbPb}/(K^{*}[±]/ π)_{pp} are suppressed by up to a factor of five. The suppression is stronger in central collisions than peripheral ones due to a stronger rescattering effect in the larger system produced in the central collisions. For p_T (> 5 GeV/c), the double ratios are consistent with unity for both central and peripheral collisions, suggesting that the rescattering effect is a low p_T phenomenon. The lower panels of Figure 7 (c and d) present the comparison of results for K^{*}[±] and K^{*}⁰ [39] in the 0–10% centrality interval, demonstrating their consistency with each other. In the intermediate p_T range (3–5 GeV/c), both the double ratios (c and d) show an enhancement in central Pb–Pb collisions compared with peripheral and pp collisions. This enhancement is more pronounced for K^{*}[±]/ π yield ratio and is consistent with the picture of larger radial flow in the most central collisions relative to peripheral and pp collisions.

4.5 Nuclear modification factor

The left panel of Fig. 8 shows the species dependence of R_{AA} for 0–10% Pb–Pb collisions at $\sqrt{s_{\text{NN}}} = 5.02 \text{ TeV}$. The species vary in mass from 0.139 GeV/c² for pions to 1.020 GeV/c² for the ϕ meson. Both baryons and mesons have been considered. At low p_T (< 2 GeV/c), K^{*}[±] and K^{*}⁰ R_{AA} values are the smallest among the listed hadrons, which is consistent with the picture of the rescattering effect. R_{AA} values in the intermediate p_T range show species dependence with evidence of baryon–meson splitting. R_{AA} values in this p_T range are influenced by a combination of effects like radial flow, parton recombination, enhanced strangeness production, steepness of particle p_T spectra in reference pp collisions, etc., which are difficult to disentangle from R_{AA} measurements alone. For $p_T > 8 \text{ GeV}/c$, all the particle species show similar R_{AA} within the uncertainties, including the K^{*}[±]. This observation suggests that suppression of various light flavored hadrons is independent of their quark content and mass. The

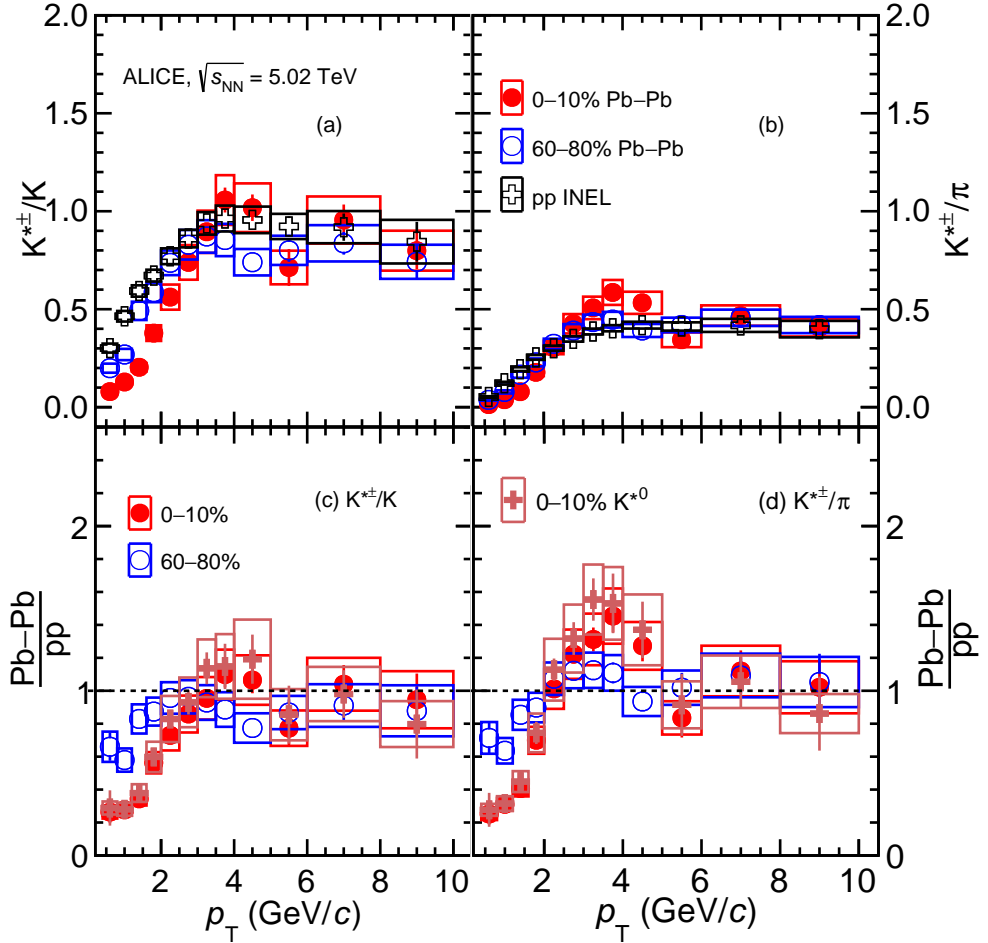


Figure 7: The p_T -differential particle yield ratios $K^{*\pm}/K$ (a) and $K^{*\pm}/\pi$ (b) in pp (black marker) and Pb–Pb collisions at $\sqrt{s_{\text{NN}}} = 5.02$ TeV for 0–10% (red marker) and 60–80% (blue marker) centrality intervals. The bottom panels (c) and (d) show the ratios of Pb–Pb to pp results, compared with 0–10% K^{*0} results [39]. Statistical uncertainties are shown by bars and systematic uncertainties by boxes. The statistical and systematic uncertainties on the data points are obtained by propagating the statistical and total systematic uncertainties of the measurements.

right panel of Fig. 8 shows the evolution of R_{AA} values with centrality for $K^{*\pm}$. The R_{AA} is found to be the smallest in most central collisions. It gradually increases towards more peripheral collisions similarly for other light hadrons. The results are consistent with centrality-dependent energy loss of partons.

5 Conclusion

The first measurement of $K^{*\pm}$ resonance in Pb–Pb collisions at $\sqrt{s_{\text{NN}}} = 5.02$ TeV using the ALICE detector has been presented. The transverse-momentum spectra are measured at midrapidity up to $p_T = 16$ GeV/ c in various centrality intervals. A good consistency between the presented $K^{*\pm}$ results and the previously published K^{*0} measurements is observed. The p_T -integrated yields and $\langle p_T \rangle$ values for $K^{*\pm}$ and K^{*0} at $\sqrt{s_{\text{NN}}} = 5.02$ TeV and $\sqrt{s_{\text{NN}}} = 2.76$ TeV exhibit a common smooth evolution with event multiplicity. A suppression is observed in the $K^{*\pm}/K$ yield ratio in central Pb–Pb collisions compared with peripheral Pb–Pb collisions and pp collisions. The measured suppression of the $K^{*\pm}/K$ ratio is observed to be akin to that of K^{*0}/K , albeit with higher precision (9.3σ as opposed to 6.02σ). A suppression factor of about five is observed for K^{*}/K at low p_T . These observations indicate the dominance of rescattering effect over regeneration at low p_T in the hadronic phase of the system produced in heavy-ion collisions, which is consistent with the observations made from K^{*0} measurements at $\sqrt{s_{\text{NN}}} = 5.02$ TeV

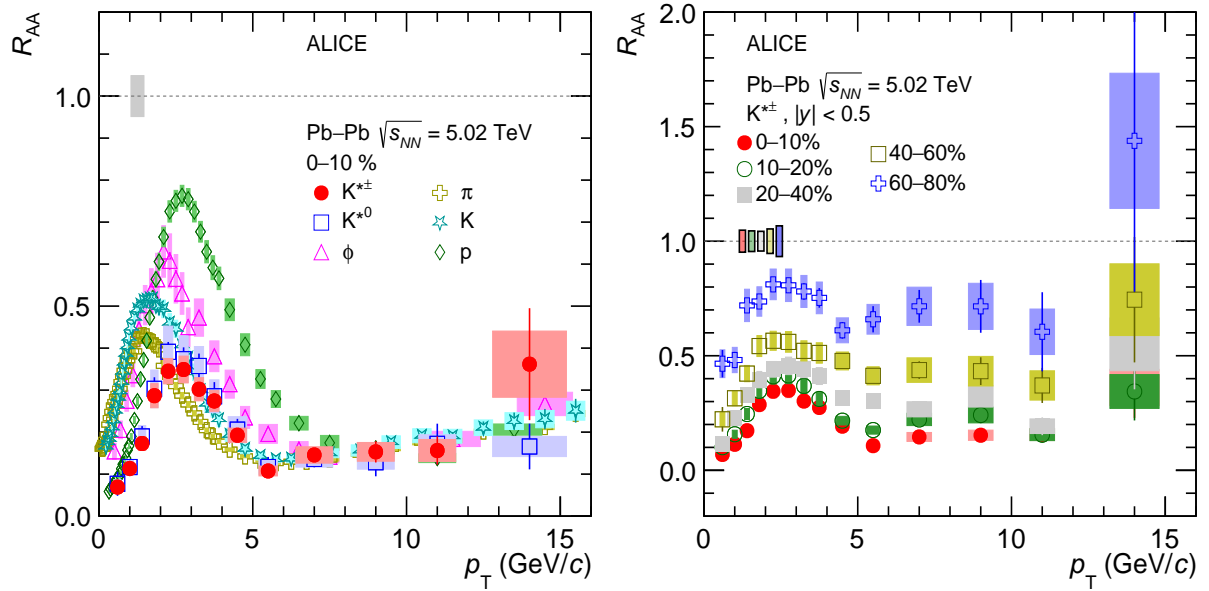


Figure 8: Left panel shows the R_{AA} comparison of various light-flavored hadrons [39, 40, 57], and the right panel shows the R_{AA} of $K^{*\pm}$ for different centrality intervals both as a function of p_T in Pb–Pb collisions at $\sqrt{s_{NN}} = 5.02$ TeV. Statistical (systematic) uncertainties are shown by bars (shaded boxes). The shaded bands around unity represents the normalisation uncertainty on R_{AA} .

and 2.76 TeV.

The values of the p_T -integrated K^*/K ratios in Pb–Pb collisions are smaller than those obtained from thermal model predictions but qualitatively consistent with models which include a finite hadronic phase lifetime. Predictions of the hydrodynamic model MUSIC are noticeably closer to the measurements when processed with the hadronic afterburner SMASH. HRG-PCE qualitatively describes the suppression trend of K^*/K particle ratios. These observations emphasize the importance of the hadronic phase in central heavy-ion collisions. The kinetic freeze-out temperature is determined in different centrality intervals using the HRG-PCE model fit to the experimental data at a fixed chemical freeze-out temperature. The results suggest a longer-lived hadronic phase in central collisions as compared with peripheral collisions. The kinetic freeze-out temperature results are consistent with predictions obtained from blast-wave fits to pion, kaon, and proton p_T spectra.

The values of the nuclear modification factor (R_{AA}) for K^* are below unity at all centralities and are consistent with energy loss of partons while traversing the hot and dense medium. The R_{AA} values are smaller in most central collisions and increase towards peripheral collisions. No species dependence is observed at high p_T .

Acknowledgements

The ALICE Collaboration would like to thank all its engineers and technicians for their invaluable contributions to the construction of the experiment and the CERN accelerator teams for the outstanding performance of the LHC complex. The ALICE Collaboration gratefully acknowledges the resources and support provided by all Grid centres and the Worldwide LHC Computing Grid (WLCG) collaboration. The ALICE Collaboration acknowledges the following funding agencies for their support in building and running the ALICE detector: A. I. Alikhanyan National Science Laboratory (Yerevan Physics Institute) Foundation (ANSL), State Committee of Science and World Federation of Scientists (WFS), Armenia; Austrian Academy of Sciences, Austrian Science Fund (FWF): [M 2467-N36] and Nationalstiftung für Forschung, Technologie und Entwicklung, Austria; Ministry of Communications and High Technologies, National Nuclear Research Center, Azerbaijan; Conselho Nacional de Desenvolvimento

Científico e Tecnológico (CNPq), Financiadora de Estudos e Projetos (Finep), Fundação de Amparo à Pesquisa do Estado de São Paulo (FAPESP) and Universidade Federal do Rio Grande do Sul (UFRGS), Brazil; Bulgarian Ministry of Education and Science, within the National Roadmap for Research Infrastructures 2020–2027 (object CERN), Bulgaria; Ministry of Education of China (MOEC) , Ministry of Science & Technology of China (MSTC) and National Natural Science Foundation of China (NSFC), China; Ministry of Science and Education and Croatian Science Foundation, Croatia; Centro de Aplicaciones Tecnológicas y Desarrollo Nuclear (CEADEN), Cubaenergía, Cuba; Ministry of Education, Youth and Sports of the Czech Republic, Czech Republic; The Danish Council for Independent Research | Natural Sciences, the VILLUM FONDEN and Danish National Research Foundation (DNRF), Denmark; Helsinki Institute of Physics (HIP), Finland; Commissariat à l’Energie Atomique (CEA) and Institut National de Physique Nucléaire et de Physique des Particules (IN2P3) and Centre National de la Recherche Scientifique (CNRS), France; Bundesministerium für Bildung und Forschung (BMBF) and GSI Helmholtzzentrum für Schwerionenforschung GmbH, Germany; General Secretariat for Research and Technology, Ministry of Education, Research and Religions, Greece; National Research, Development and Innovation Office, Hungary; Department of Atomic Energy Government of India (DAE), Department of Science and Technology, Government of India (DST), University Grants Commission, Government of India (UGC) and Council of Scientific and Industrial Research (CSIR), India; National Research and Innovation Agency - BRIN, Indonesia; Istituto Nazionale di Fisica Nucleare (INFN), Italy; Japanese Ministry of Education, Culture, Sports, Science and Technology (MEXT) and Japan Society for the Promotion of Science (JSPS) KAKENHI, Japan; Consejo Nacional de Ciencia (CONACYT) y Tecnología, through Fondo de Cooperación Internacional en Ciencia y Tecnología (FONCICYT) and Dirección General de Asuntos del Personal Académico (DGAPA), Mexico; Nederlandse Organisatie voor Wetenschappelijk Onderzoek (NWO), Netherlands; The Research Council of Norway, Norway; Commission on Science and Technology for Sustainable Development in the South (COMSATS), Pakistan; Pontificia Universidad Católica del Perú, Peru; Ministry of Education and Science, National Science Centre and WUT ID-UB, Poland; Korea Institute of Science and Technology Information and National Research Foundation of Korea (NRF), Republic of Korea; Ministry of Education and Scientific Research, Institute of Atomic Physics, Ministry of Research and Innovation and Institute of Atomic Physics and University Politehnica of Bucharest, Romania; Ministry of Education, Science, Research and Sport of the Slovak Republic, Slovakia; National Research Foundation of South Africa, South Africa; Swedish Research Council (VR) and Knut & Alice Wallenberg Foundation (KAW), Sweden; European Organization for Nuclear Research, Switzerland; Suranaree University of Technology (SUT), National Science and Technology Development Agency (NSTDA), Thailand Science Research and Innovation (TSRI) and National Science, Research and Innovation Fund (NSRF), Thailand; Turkish Energy, Nuclear and Mineral Research Agency (TENMAK), Turkey; National Academy of Sciences of Ukraine, Ukraine; Science and Technology Facilities Council (STFC), United Kingdom; National Science Foundation of the United States of America (NSF) and United States Department of Energy, Office of Nuclear Physics (DOE NP), United States of America. In addition, individual groups or members have received support from: European Research Council, Strong 2020 - Horizon 2020 (grant nos. 950692, 824093), European Union; Academy of Finland (Center of Excellence in Quark Matter) (grant nos. 346327, 346328), Finland.

References

- [1] STAR Collaboration, K. H. Ackermann *et al.*, “Elliptic flow in Au+Au collisions at $\sqrt{s_{\text{NN}}} = 130$ GeV”, *Phys. Rev. Lett.* **86** (2001) 402–407, arXiv:nucl-ex/0009011.
- [2] STAR Collaboration, J. Adams *et al.*, “Experimental and theoretical challenges in the search for the quark gluon plasma: The STAR Collaboration’s critical assessment of the evidence from RHIC collisions”, *Nucl. Phys. A* **757** (2005) 102–183, arXiv:nucl-ex/0501009.

- [3] **STAR** Collaboration, J. Adams *et al.*, “Evidence from d+Au measurements for final state suppression of high p_{T} hadrons in Au+Au collisions at RHIC”, *Phys. Rev. Lett.* **91** (2003) 072304, arXiv:nucl-ex/0306024.
- [4] **STAR** Collaboration, C. Adler *et al.*, “Disappearance of back-to-back high p_{T} hadron correlations in central Au+Au collisions at $\sqrt{s_{\text{NN}}} = 200$ GeV”, *Phys. Rev. Lett.* **90** (2003) 082302, arXiv:nucl-ex/0210033.
- [5] **STAR** Collaboration, J. Adams *et al.*, “Particle type dependence of azimuthal anisotropy and nuclear modification of particle production in Au+Au collisions at $\sqrt{s_{\text{NN}}} = 200$ GeV”, *Phys. Rev. Lett.* **92** (2004) 052302, arXiv:nucl-ex/0306007.
- [6] **PHENIX** Collaboration, K. Adcox *et al.*, “Suppression of hadrons with large transverse momentum in central Au+Au collisions at $\sqrt{s_{\text{NN}}} = 130$ GeV”, *Phys. Rev. Lett.* **88** (2002) 022301, arXiv:nucl-ex/0109003.
- [7] **PHENIX** Collaboration, K. Adcox *et al.*, “Formation of dense partonic matter in relativistic nucleus-nucleus collisions at RHIC: Experimental evaluation by the PHENIX collaboration”, *Nucl. Phys. A* **757** (2005) 184–283, arXiv:nucl-ex/0410003.
- [8] **BRAHMS** Collaboration, I. Arsene *et al.*, “Quark gluon plasma and color glass condensate at RHIC? The Perspective from the BRAHMS experiment”, *Nucl. Phys. A* **757** (2005) 1–27, arXiv:nucl-ex/0410020.
- [9] **PHOBOS** Collaboration, B. B. Back *et al.*, “The PHOBOS perspective on discoveries at RHIC”, *Nucl. Phys. A* **757** (2005) 28–101, arXiv:nucl-ex/0410022.
- [10] **ALICE** Collaboration, “The ALICE experiment – A journey through QCD”, arXiv:2211.04384 [nucl-ex].
- [11] **ALICE** Collaboration, K. Aamodt *et al.*, “Elliptic flow of charged particles in Pb–Pb collisions at 2.76 TeV”, *Phys. Rev. Lett.* **105** (2010) 252302, arXiv:1011.3914 [nucl-ex].
- [12] **ALICE** Collaboration, K. Aamodt *et al.*, “Suppression of Charged Particle Production at Large Transverse Momentum in Central Pb–Pb Collisions at $\sqrt{s_{\text{NN}}}=2.76$ TeV”, *Phys. Lett. B* **696** (2011) 30–39, arXiv:1012.1004 [nucl-ex].
- [13] **ALICE** Collaboration, K. Aamodt *et al.*, “Higher harmonic anisotropic flow measurements of charged particles in Pb–Pb collisions at $\sqrt{s_{\text{NN}}}=2.76$ TeV”, *Phys. Rev. Lett.* **107** (2011) 032301, arXiv:1105.3865 [nucl-ex].
- [14] U. W. Heinz, “The Strongly coupled quark-gluon plasma created at RHIC”, *J. Phys. A* **42** (2009) 214003, arXiv:0810.5529 [nucl-th].
- [15] T. Niida and Y. Miake, “Signatures of QGP at RHIC and the LHC”, *AAPPS Bull.* **31** (2021) 12, arXiv:2104.11406 [nucl-ex].
- [16] J. P. Blaizot and J.-Y. Ollitrault, “Equation of State and Hydrodynamics of Quark Gluon Plasmas”, *Phys. Lett. B* **191** (1987) 21–26.
- [17] D. A. Teaney, *Viscous Hydrodynamics and the Quark Gluon Plasma*, pp. 207–266. 2010. arXiv:0905.2433 [nucl-th].
- [18] B. Schenke, S. Jeon, and C. Gale, “Elliptic and triangular flow in event-by-event (3+1)D viscous hydrodynamics”, *Phys. Rev. Lett.* **106** (2011) 042301, arXiv:1009.3244 [hep-ph].

- [19] J.-Y. Ollitrault, “Anisotropy as a signature of transverse collective flow”, *Phys. Rev. D* **46** (1992) 229–245.
- [20] J. D. Bjorken, “Highly Relativistic Nucleus-Nucleus Collisions: The Central Rapidity Region”, *Phys. Rev. D* **27** (1983) 140–151.
- [21] D. Teaney, J. Lauret, and E. V. Shuryak, “Flow at the SPS and RHIC as a quark gluon plasma signature”, *Phys. Rev. Lett.* **86** (2001) 4783–4786, arXiv:nucl-th/0011058.
- [22] A. Jaiswal and V. Roy, “Relativistic hydrodynamics in heavy-ion collisions: general aspects and recent developments”, *Adv. High Energy Phys.* **2016** (2016) 9623034, arXiv:1605.08694 [nucl-th].
- [23] M. L. Miller, K. Reygers, S. J. Sanders, and P. Steinberg, “Glauber modeling in high energy nuclear collisions”, *Ann. Rev. Nucl. Part. Sci.* **57** (2007) 205–243, arXiv:nucl-ex/0701025.
- [24] B. Schenke, C. Shen, and P. Tribedy, “Hybrid Color Glass Condensate and hydrodynamic description of the Relativistic Heavy Ion Collider small system scan”, *Phys. Lett. B* **803** (2020) 135322, arXiv:1908.06212 [nucl-th].
- [25] J. Liu, C. Shen, and U. Heinz, “Pre-equilibrium evolution effects on heavy-ion collision observables”, *Phys. Rev. C* **91** (2015) 064906, arXiv:1504.02160 [nucl-th]. [Erratum: Phys.Rev.C 92, 049904 (2015)].
- [26] B. Schenke, P. Tribedy, and R. Venugopalan, “Fluctuating Glasma initial conditions and flow in heavy ion collisions”, *Phys. Rev. Lett.* **108** (2012) 252301, arXiv:1202.6646 [nucl-th].
- [27] A. Andronic, P. Braun-Munzinger, K. Redlich, and J. Stachel, “Decoding the phase structure of QCD via particle production at high energy”, *Nature* **561** (2018) 321–330, arXiv:1710.09425 [nucl-th].
- [28] **HotQCD** Collaboration, A. Bazavov *et al.*, “Chiral crossover in QCD at zero and non-zero chemical potentials”, *Phys. Lett. B* **795** (2019) 15–21, arXiv:1812.08235 [hep-lat].
- [29] V. Greco, C. M. Ko, and P. Levai, “Parton coalescence and anti-proton / pion anomaly at RHIC”, *Phys. Rev. Lett.* **90** (2003) 202302, arXiv:nucl-th/0301093.
- [30] V. Greco, C. M. Ko, and P. Levai, “Parton coalescence at RHIC”, *Phys. Rev. C* **68** (2003) 034904, arXiv:nucl-th/0305024.
- [31] R. J. Fries, B. Muller, C. Nonaka, and S. A. Bass, “Hadronization in heavy ion collisions: Recombination and fragmentation of partons”, *Phys. Rev. Lett.* **90** (2003) 202303, arXiv:nucl-th/0301087.
- [32] R. J. Fries, B. Muller, C. Nonaka, and S. A. Bass, “Hadron production in heavy ion collisions: Fragmentation and recombination from a dense parton phase”, *Phys. Rev. C* **68** (2003) 044902, arXiv:nucl-th/0306027.
- [33] D. Teaney, “Chemical freezeout in heavy ion collisions”, arXiv:nucl-th/0204023.
- [34] J. Manninen and F. Becattini, “Chemical freeze-out in ultra-relativistic heavy ion collisions at $\sqrt{s_{\text{NN}}} = 130$ and 200 GeV”, *Phys. Rev. C* **78** (2008) 054901, arXiv:0806.4100 [nucl-th].
- [35] U. W. Heinz and G. Kestin, “Jozso’s Legacy: Chemical and Kinetic Freeze-out in Heavy-Ion Collisions”, *Eur. Phys. J. ST* **155** (2008) 75–87, arXiv:0709.3366 [nucl-th].

- [36] J. Steinheimer, J. Aichelin, M. Bleicher, and H. Stöcker, “Influence of the hadronic phase on observables in ultrarelativistic heavy ion collisions”, *Phys. Rev. C* **95** (2017) 064902, arXiv:1703.06638 [nucl-th].
- [37] G. Torrieri and J. Rafelski, “Strange hadron resonances as a signature of freezeout dynamics”, *Phys. Lett. B* **509** (2001) 239–245, arXiv:hep-ph/0103149.
- [38] C. Markert, “What do we learn from resonance production in heavy ion collisions?”, *J. Phys. G* **31** (2005) S169–S178, arXiv:nucl-ex/0503013.
- [39] **ALICE** Collaboration, S. Acharya *et al.*, “Production of K^{*}(892)⁰ and $\phi(1020)$ in pp and Pb–Pb collisions at $\sqrt{s_{\text{NN}}} = 5.02$ TeV”, *Phys. Rev. C* **106** (2022) 034907, arXiv:2106.13113 [nucl-ex].
- [40] **ALICE** Collaboration, B. Abelev *et al.*, “K^{*}(892)⁰ and $\phi(1020)$ production in Pb–Pb collisions at $\sqrt{s_{\text{NN}}} = 2.76$ TeV”, *Phys. Rev. C* **91** (2015) 024609, arXiv:1404.0495 [nucl-ex].
- [41] **NA49** Collaboration, C. Alt *et al.*, “Energy dependence of ϕ meson production in central Pb+Pb collisions at $\sqrt{s_{\text{NN}}} = 6$ to 17 GeV”, *Phys. Rev. C* **78** (2008) 044907, arXiv:0806.1937 [nucl-ex].
- [42] **NA49** Collaboration, S. V. Afanasiev *et al.*, “Production of ϕ mesons in p+p, p+Pb and central Pb+Pb collisions at E(beam) = 158 A GeV”, *Phys. Lett. B* **491** (2000) 59–66.
- [43] **NA49** Collaboration, T. Anticic *et al.*, “K^{*}(892)⁰ and $\bar{K}^*(892)^0$ production in central Pb+Pb, Si+Si, C+C and inelastic p+p collisions at 158 A GeV”, *Phys. Rev. C* **84** (2011) 064909, arXiv:1105.3109 [nucl-ex].
- [44] **PHENIX** Collaboration, A. Adare *et al.*, “Measurement of K_S⁰ and K^{*0} in p+p, d+Au, and Cu+Cu collisions at $\sqrt{s_{\text{NN}}} = 200$ GeV”, *Phys. Rev. C* **90** (2014) 054905, arXiv:1405.3628 [nucl-ex].
- [45] **PHENIX** Collaboration, N. J. Abdulameer *et al.*, “Measurement of ϕ -meson production in Cu+Au collisions at $\sqrt{s_{\text{NN}}} = 200$ GeV and U+U collisions at $\sqrt{s_{\text{NN}}} = 193$ GeV”, *Phys. Rev. C* **107** (2023) 014907, arXiv:2207.10745 [nucl-ex].
- [46] **PHENIX** Collaboration, U. Acharya *et al.*, “Study of ϕ meson production in p+Al, p+Au, d+Au, and ³He+Au collisions at $\sqrt{s_{\text{NN}}} = 200$ GeV”, *Phys. Rev. C* **106** (2022) 014908, arXiv:2203.06087 [nucl-ex].
- [47] **PHENIX** Collaboration, S. S. Adler *et al.*, “Production of ϕ mesons at mid-rapidity in $\sqrt{s_{\text{NN}}} = 200$ GeV Au+Au collisions at RHIC”, *Phys. Rev. C* **72** (2005) 014903, arXiv:nucl-ex/0410012.
- [48] **STAR** Collaboration, B. I. Abelev *et al.*, “Energy and system size dependence of ϕ meson production in Cu+Cu and Au+Au collisions”, *Phys. Lett. B* **673** (2009) 183–191, arXiv:0810.4979 [nucl-ex].
- [49] **STAR** Collaboration, B. I. Abelev *et al.*, “Measurements of ϕ meson production in relativistic heavy-ion collisions at RHIC”, *Phys. Rev. C* **79** (2009) 064903, arXiv:0809.4737 [nucl-ex].
- [50] **STAR** Collaboration, C. Adler *et al.*, “K^{*}(892)⁰ production in relativistic heavy ion collisions at $\sqrt{s_{\text{NN}}} = 130$ GeV”, *Phys. Rev. C* **66** (2002) 061901, arXiv:nucl-ex/0205015.
- [51] **STAR** Collaboration, J. Adams *et al.*, “K^{*}(892) resonance production in Au+Au and p+p collisions at $\sqrt{s_{\text{NN}}} = 200$ GeV at STAR”, *Phys. Rev. C* **71** (2005) 064902, arXiv:nucl-ex/0412019.

- [52] **STAR** Collaboration, M. M. Aggarwal *et al.*, “K⁰ production in Cu+Cu and Au+Au collisions at $\sqrt{s_{\text{NN}}} = 62.4 \text{ GeV}$ and 200 GeV”, *Phys. Rev. C* **84** (2011) 034909, arXiv:1006.1961 [nucl-ex].
- [53] S. Singha, B. Mohanty, and Z.-W. Lin, “Studying re-scattering effect in heavy-ion collision through K^{*} production”, *Int. J. Mod. Phys. E* **24** (2015) 1550041, arXiv:1505.02342 [nucl-ex].
- [54] **ALICE** Collaboration, S. Acharya *et al.*, “Evidence of rescattering effect in Pb–Pb collisions at the LHC through production of K^{*(892)0} and $\phi(1020)$ mesons”, *Phys. Lett. B* **802** (2020) 135225, arXiv:1910.14419 [nucl-ex].
- [55] C. Loizides, J. Nagle, and P. Steinberg, “Improved version of the PHOBOS Glauber Monte Carlo”, *SoftwareX* **1-2** (2015) 13–18, arXiv:1408.2549 [nucl-ex].
- [56] **ALICE** Collaboration, S. Acharya *et al.*, “Production of charged pions, kaons, and (anti-)protons in Pb–Pb and inelastic pp collisions at $\sqrt{s_{\text{NN}}} = 5.02 \text{ TeV}$ ”, *Phys. Rev. C* **101** (2020) 044907, arXiv:1910.07678 [nucl-ex].
- [57] **ALICE** Collaboration, B. Abelev *et al.*, “Production of charged pions, kaons and protons at large transverse momenta in pp and Pb–Pb collisions at $\sqrt{s_{\text{NN}}} = 2.76 \text{ TeV}$ ”, *Phys. Lett. B* **736** (2014) 196–207, arXiv:1401.1250 [nucl-ex].
- [58] **ALICE** Collaboration, J. Adam *et al.*, “Centrality dependence of the nuclear modification factor of charged pions, kaons, and protons in Pb–Pb collisions at $\sqrt{s_{\text{NN}}} = 2.76 \text{ TeV}$ ”, *Phys. Rev. C* **93** (2016) 034913, arXiv:1506.07287 [nucl-ex].
- [59] A. Motornenko, V. Vovchenko, C. Greiner, and H. Stoecker, “Kinetic freeze-out temperature from yields of short-lived resonances”, *Phys. Rev. C* **102** (2020) 024909, arXiv:1908.11730 [hep-ph].
- [60] **ALICE** Collaboration, K. Aamodt *et al.*, “The ALICE experiment at the CERN LHC”, *JINST* **3** (2008) S08002.
- [61] **ALICE** Collaboration, B. Abelev *et al.*, “Performance of the ALICE Experiment at the CERN LHC”, *Int. J. Mod. Phys. A* **29** (2014) 1430044, arXiv:1402.4476 [nucl-ex].
- [62] **ALICE** Collaboration, K. Aamodt *et al.*, “Alignment of the ALICE Inner Tracking System with cosmic-ray tracks”, *JINST* **5** (2010) P03003, arXiv:1001.0502 [physics.ins-det].
- [63] J. Alme *et al.*, “The ALICE TPC, a large 3-dimensional tracking device with fast readout for ultra-high multiplicity events”, *Nucl. Instrum. Meth. A* **622** (2010) 316–367, arXiv:1001.1950 [physics.ins-det].
- [64] **ALICE** Collaboration, G. Dellacasa *et al.*, “ALICE technical design report of the time-of-flight system (TOF)”, *CERN-LHCC-2000-012*.
- [65] **ALICE** Collaboration, P. Cortese *et al.*, “ALICE: Addendum to the technical design report of the time of flight system (TOF)”, *CERN-LHCC-2002-016*.
- [66] **ALICE** Collaboration, E. Abbas *et al.*, “Performance of the ALICE VZERO system”, *JINST* **8** (2013) P10016, arXiv:1306.3130 [nucl-ex].
- [67] **Particle Data Group** Collaboration, P. A. Zyla *et al.*, “Review of Particle Physics”, *PTEP* **2020** (2020) 083C01.

- [68] ALICE Collaboration, F. Carnesecchi, “Performance of the ALICE Time-Of-Flight detector at the LHC”, *JINST* **14** (2019) C06023, arXiv:1806.03825 [physics.ins-det].
- [69] ALICE Collaboration, S. Acharya *et al.*, “Measurement of K^{*}(892)[±] production in inelastic pp collisions at the LHC”, *Phys. Lett. B* **828** (2022) 137013, arXiv:2105.05760 [nucl-ex].
- [70] X.-N. Wang and M. Gyulassy, “HIJING: A Monte Carlo model for multiple jet production in pp, pA and AA collisions”, *Phys. Rev. D* **44** (1991) 3501–3516.
- [71] R. Brun, F. Bruyant, F. Carminati, S. Giani, M. Maire, A. McPherson, G. Patrick, and L. Urban, “GEANT Detector Description and Simulation Tool”, *CERN Program Library, CERN, Geneva* (1993).
- [72] E. Schnedermann, J. Sollfrank, and U. W. Heinz, “Thermal phenomenology of hadrons from 200-A/GeV S+S collisions”, *Phys. Rev. C* **48** (1993) 2462–2475, arXiv:nucl-th/9307020.
- [73] C. Tsallis, “Possible Generalization of Boltzmann-Gibbs Statistics”, *J. Statist. Phys.* **52** (1988) 479–487.
- [74] ALICE Collaboration, S. Acharya *et al.*, “Production of light-flavor hadrons in pp collisions at $\sqrt{s} = 7$ and $\sqrt{s} = 13$ TeV”, *Eur. Phys. J. C* **81** (2021) 256, arXiv:2005.11120 [nucl-ex].
- [75] D. Oliinychenko and C. Shen, “Resonance production in PbPb collisions at 5.02 TeV via hydrodynamics and hadronic afterburner”, arXiv:2105.07539 [hep-ph].
- [76] J. Weil *et al.*, “Particle production and equilibrium properties within a new hadron transport approach for heavy-ion collisions”, *Phys. Rev. C* **94** (2016) 054905, arXiv:1606.06642 [nucl-th].
- [77] ALICE Collaboration, B. Abelev *et al.*, “Centrality dependence of π , K, p production in Pb–Pb collisions at $\sqrt{s_{\text{NN}}} = 2.76$ TeV”, *Phys. Rev. C* **88** (2013) 044910, arXiv:1303.0737 [hep-ex].
- [78] V. Vovchenko and H. Stoecker, “Thermal-FIST: A package for heavy-ion collisions and hadronic equation of state”, *Comput. Phys. Commun.* **244** (2019) 295–310, arXiv:1901.05249 [nucl-th].
- [79] V. Vovchenko, B. Dönigus, and H. Stoecker, “Canonical statistical model analysis of pp, p–Pb, and Pb–Pb collisions at energies available at the CERN Large Hadron Collider”, *Phys. Rev. C* **100** (2019) 054906, arXiv:1906.03145 [hep-ph].

A The ALICE Collaboration

S. Acharya ¹²⁸, D. Adamová ⁸⁷, G. Aglieri Rinella ³³, M. Agnello ³⁰, N. Agrawal ⁵², Z. Ahammed ¹³⁶, S. Ahmad ¹⁶, S.U. Ahn ⁷², I. Ahuja ³⁸, A. Akindinov ¹⁴², M. Al-Turany ⁹⁸, D. Aleksandrov ¹⁴², B. Alessandro ⁵⁷, H.M. Alfanda ⁶, R. Alfaro Molina ⁶⁸, B. Ali ¹⁶, A. Alici ²⁶, N. Alizadehvandchali ¹¹⁷, A. Alkin ³³, J. Alme ²¹, G. Alocco ⁵³, T. Alt ⁶⁵, A.R. Altamura ⁵¹, I. Altsybeev ⁹⁶, J.R. Alvarado ⁴⁵, M.N. Anaam ⁶, C. Andrei ⁴⁶, N. Andreou ¹¹⁶, A. Andronic ¹²⁷, V. Anguelov ⁹⁵, F. Antinori ⁵⁵, P. Antonioli ⁵², N. Apadula ⁷⁵, L. Aphecetche ¹⁰⁴, H. Appelshäuser ⁶⁵, C. Arata ⁷⁴, S. Arcelli ²⁶, M. Aresti ²³, R. Arnaldi ⁵⁷, J.G.M.C.A. Arneiro ¹¹¹, I.C. Arsene ²⁰, M. Arslanbekov ¹³⁹, A. Augustinus ³³, R. Averbeck ⁹⁸, M.D. Azmi ¹⁶, H. Baba ¹²⁵, A. Badalà ⁵⁴, J. Bae ¹⁰⁵, Y.W. Baek ⁴¹, X. Bai ¹²¹, R. Bailhache ⁶⁵, Y. Bailung ⁴⁹, A. Balbino ³⁰, A. Baldissari ¹³¹, B. Balis ², D. Banerjee ⁴, Z. Banoo ⁹², R. Barbera ²⁷, F. Barile ³², L. Barioglio ⁹⁶, M. Barlou ⁷⁹, B. Barman ⁴², G.G. Barnaföldi ⁴⁷, L.S. Barnby ⁸⁶, V. Barret ¹²⁸, L. Barreto ¹¹¹, C. Bartels ¹²⁰, K. Barth ³³, E. Bartsch ⁶⁵, N. Bastid ¹²⁸, S. Basu ⁷⁶, G. Batigne ¹⁰⁴, D. Battistini ⁹⁶, B. Batyunya ¹⁴³, D. Bauri ⁴⁸, J.L. Bazo Alba ¹⁰², I.G. Bearden ⁸⁴, C. Beattie ¹³⁹, P. Becht ⁹⁸, D. Behera ⁴⁹, I. Belikov ¹³⁰, A.D.C. Bell Hechavarria ¹²⁷, F. Bellini ²⁶, R. Bellwied ¹¹⁷, S. Belokurova ¹⁴², Y.A.V. Beltran ⁴⁵, G. Bencedi ⁴⁷, S. Beole ²⁵, Y. Berdnikov ¹⁴², A. Berdnikova ⁹⁵, L. Bergmann ⁹⁵, M.G. Besoiu ⁶⁴, L. Betev ³³, P.P. Bhaduri ¹³⁶, A. Bhasin ⁹², M.A. Bhat ⁴, B. Bhattacharjee ⁴², L. Bianchi ²⁵, N. Bianchi ⁵⁰, J. Bielčík ³⁶, J. Bielčíková ⁸⁷, J. Biernat ¹⁰⁸, A.P. Bigot ¹³⁰, A. Bilandzic ⁹⁶, G. Biro ⁴⁷, S. Biswas ⁴, N. Bize ¹⁰⁴, J.T. Blair ¹⁰⁹, D. Blau ¹⁴², M.B. Blidaru ⁹⁸, N. Bluhme ³⁹, C. Blume ⁶⁵, G. Boca ^{22,56}, F. Bock ⁸⁸, T. Bodova ²¹, A. Bogdanov ¹⁴², S. Boi ²³, J. Bok ⁵⁹, L. Boldizsár ⁴⁷, M. Bombara ³⁸, P.M. Bond ³³, G. Bonomi ^{135,56}, H. Borel ¹³¹, A. Borissov ¹⁴², A.G. Borquez Carcamo ⁹⁵, H. Bossi ¹³⁹, E. Botta ²⁵, Y.E.M. Bouziani ⁶⁵, L. Bratrud ⁶⁵, P. Braun-Munzinger ⁹⁸, M. Bregant ¹¹¹, M. Broz ³⁶, G.E. Bruno ^{97,32}, M.D. Buckland ²⁴, D. Budnikov ¹⁴², H. Buesching ⁶⁵, S. Bufalino ³⁰, P. Buhler ¹⁰³, N. Burmasov ¹⁴², Z. Buthelezi ^{69,124}, A. Bylinkin ²¹, S.A. Bysiak ¹⁰⁸, M. Cai ⁶, H. Caines ¹³⁹, A. Caliva ²⁹, E. Calvo Villar ¹⁰², J.M.M. Camacho ¹¹⁰, P. Camerini ²⁴, F.D.M. Canedo ¹¹¹, S.L. Cantway ¹³⁹, M. Carabas ¹¹⁴, A.A. Carballo ³³, F. Carnesecchi ³³, R. Caron ¹²⁹, L.A.D. Carvalho ¹¹¹, J. Castillo Castellanos ¹³¹, F. Catalano ^{33,25}, C. Ceballos Sanchez ¹⁴³, I. Chakaberia ⁷⁵, P. Chakraborty ⁴⁸, S. Chandra ¹³⁶, S. Chapeland ³³, M. Chartier ¹²⁰, S. Chattopadhyay ¹³⁶, S. Chattopadhyay ¹⁰⁰, T. Cheng ^{98,6}, C. Cheshkov ¹²⁹, B. Cheynis ¹²⁹, V. Chibante Barroso ³³, D.D. Chinellato ¹¹², E.S. Chizzali ^{II,96}, J. Cho ⁵⁹, S. Cho ⁵⁹, P. Chochula ³³, D. Choudhury ⁴², P. Christakoglou ⁸⁵, C.H. Christensen ⁸⁴, P. Christiansen ⁷⁶, T. Chujo ¹²⁶, M. Ciacco ³⁰, C. Cicalo ⁵³, F. Cindolo ⁵², M.R. Ciupek ⁹⁸, G. Clai III,52, F. Colamaria ⁵¹, J.S. Colburn ¹⁰¹, D. Colella ^{97,32}, M. Colocci ²⁶, M. Concias ^{IV,33}, G. Conesa Balbastre ⁷⁴, Z. Conesa del Valle ¹³², G. Contin ²⁴, J.G. Contreras ³⁶, M.L. Coquet ¹³¹, P. Cortese ^{134,57}, M.R. Cosentino ¹¹³, F. Costa ³³, S. Costanza ^{22,56}, C. Cot ¹³², J. Crkovská ⁹⁵, P. Crochet ¹²⁸, R. Cruz-Torres ⁷⁵, P. Cui ⁶, A. Dainese ⁵⁵, M.C. Danisch ⁹⁵, A. Danu ⁶⁴, P. Das ⁸¹, P. Das ⁴, S. Das ⁴, A.R. Dash ¹²⁷, S. Dash ⁴⁸, A. De Caro ²⁹, G. de Cataldo ⁵¹, J. de Cuveland ³⁹, A. De Falco ²³, D. De Gruttola ²⁹, N. De Marco ⁵⁷, C. De Martin ²⁴, S. De Pasquale ²⁹, R. Deb ¹³⁵, R. Del Grande ⁹⁶, L. Dello Stritto ²⁹, W. Deng ⁶, P. Dhankher ¹⁹, D. Di Bari ³², A. Di Mauro ³³, B. Diab ¹³¹, R.A. Diaz ^{143,7}, T. Dietel ¹¹⁵, Y. Ding ⁶, J. Ditzel ⁶⁵, R. Divià ³³, D.U. Dixit ¹⁹, Ø. Djupsland ²¹, U. Dmitrieva ¹⁴², A. Dobrin ⁶⁴, B. Dönigus ⁶⁵, J.M. Dubinski ¹³⁷, A. Dubla ⁹⁸, S. Dudi ⁹¹, P. Dupieux ¹²⁸, M. Durkac ¹⁰⁷, N. Dzalaiova ¹³, T.M. Eder ¹²⁷, R.J. Ehlers ⁷⁵, F. Eisenhut ⁶⁵, R. Ejima ⁹³, D. Elia ⁵¹, B. Erazmus ¹⁰⁴, F. Ercolelli ²⁶, B. Espagnon ¹³², G. Eulisse ³³, D. Evans ¹⁰¹, S. Evdokimov ¹⁴², L. Fabbietti ⁹⁶, M. Faggion ²⁸, J. Faivre ⁷⁴, F. Fan ⁶, W. Fan ⁷⁵, A. Fantoni ⁵⁰, M. Fasel ⁸⁸, P. Fecchio ³⁰, A. Feliciello ⁵⁷, G. Feofilov ¹⁴², A. Fernández Téllez ⁴⁵, L. Ferrandi ¹¹¹, M.B. Ferrer ³³, A. Ferrero ¹³¹, C. Ferrero ⁵⁷, A. Ferretti ²⁵, V.J.G. Feuillard ⁹⁵, V. Filova ³⁶, D. Finogeev ¹⁴², F.M. Fionda ⁵³, F. Flor ¹¹⁷, A.N. Flores ¹⁰⁹, S. Foertsch ⁶⁹, I. Fokin ⁹⁵, S. Fokin ¹⁴², E. Fragiocomo ⁵⁸, E. Frajna ⁴⁷, U. Fuchs ³³, N. Funicello ²⁹, C. Furget ⁷⁴, A. Furs ¹⁴², T. Fusayasu ⁹⁹, J.J. Gaardhøje ⁸⁴, M. Gagliardi ²⁵, A.M. Gago ¹⁰², T. Gahlaud ⁴⁸, C.D. Galvan ¹¹⁰, D.R. Gangadharan ¹¹⁷, P. Ganoti ⁷⁹, C. Garabatos ⁹⁸, T. García Chávez ⁴⁵, E. Garcia-Solis ⁹, C. Gargiulo ³³, P. Gasik ⁹⁸, A. Gautam ¹¹⁹, M.B. Gay Ducati ⁶⁷, M. Germain ¹⁰⁴, A. Ghimouz ¹²⁶, C. Ghosh ¹³⁶, M. Giacalone ⁵², G. Gioachin ³⁰, P. Giubellino ^{98,57}, P. Giubilato ²⁸, A.M.C. Glaenzer ¹³¹, P. Glässel ⁹⁵, E. Glimos ¹²³, D.J.Q. Goh ⁷⁷, V. Gonzalez ¹³⁸, M. Gorgon ², K. Goswami ⁴⁹, S. Gotovac ³⁴, V. Grabski ⁶⁸, L.K. Graczykowski ¹³⁷, E. Grecka ⁸⁷, A. Grelli ⁶⁰, C. Grigoras ³³, V. Grigoriev ¹⁴², S. Grigoryan ^{143,1}, F. Grossa ³³, J.F. Grosse-Oetringhaus ³³, R. Grossi ⁹⁸, D. Grund ³⁶, N.A. Grunwald ⁹⁵, G.G. Guardiano ¹¹², R. Guernane ⁷⁴, M. Guilbaud ¹⁰⁴, K. Gulbrandsen ⁸⁴, T. Gündem ⁶⁵, T. Gunji ¹²⁵,

W. Guo ⁶, A. Gupta ⁹², R. Gupta ⁹², R. Gupta ⁴⁹, K. Gwizdziel ¹³⁷, L. Gyulai ⁴⁷, C. Hadjidakis ¹³², F.U. Haider ⁹², S. Haidlova ³⁶, H. Hamagaki ⁷⁷, A. Hamdi ⁷⁵, Y. Han ¹⁴⁰, B.G. Hanley ¹³⁸, R. Hannigan ¹⁰⁹, J. Hansen ⁷⁶, M.R. Haque ¹³⁷, J.W. Harris ¹³⁹, A. Harton ⁹, H. Hassan ¹¹⁸, D. Hatzifotiadou ⁵², P. Hauer ⁴³, L.B. Havener ¹³⁹, S.T. Heckel ⁹⁶, E. Hellbär ⁹⁸, H. Helstrup ³⁵, M. Hemmer ⁶⁵, T. Herman ³⁶, G. Herrera Corral ⁸, F. Herrmann ¹²⁷, S. Herrmann ¹²⁹, K.F. Hetland ³⁵, B. Heybeck ⁶⁵, H. Hillemanns ³³, B. Hippolyte ¹³⁰, F.W. Hoffmann ⁷¹, B. Hofman ⁶⁰, G.H. Hong ¹⁴⁰, M. Horst ⁹⁶, A. Horzyk ², Y. Hou ⁶, P. Hristov ³³, C. Hughes ¹²³, P. Huhn ⁶⁵, L.M. Huhta ¹¹⁸, T.J. Humanic ⁸⁹, A. Hutson ¹¹⁷, D. Hutter ³⁹, R. Ilkaev ¹⁴², H. Ilyas ¹⁴, M. Inaba ¹²⁶, G.M. Innocenti ³³, M. Ippolitov ¹⁴², A. Isakov ^{85,87}, T. Isidori ¹¹⁹, M.S. Islam ¹⁰⁰, M. Ivanov ¹³, M. Ivanov ⁹⁸, V. Ivanov ¹⁴², K.E. Iversen ⁷⁶, M. Jablonski ², B. Jacak ⁷⁵, N. Jacazio ²⁶, P.M. Jacobs ⁷⁵, S. Jadlovska ¹⁰⁷, J. Jadlovsky ¹⁰⁷, S. Jaelani ⁸³, C. Jahnke ¹¹², M.J. Jakubowska ¹³⁷, M.A. Janik ¹³⁷, T. Janson ⁷¹, S. Ji ¹⁷, S. Jia ¹⁰, A.A.P. Jimenez ⁶⁶, F. Jonas ^{88,127}, D.M. Jones ¹²⁰, J.M. Jowett ^{33,98}, J. Jung ⁶⁵, M. Jung ⁶⁵, A. Junique ³³, A. Jusko ¹⁰¹, M.J. Kabus ^{33,137}, J. Kaewjai ¹⁰⁶, P. Kalinak ⁶¹, A.S. Kalteyer ⁹⁸, A. Kalweit ³³, V. Kaplin ¹⁴², A. Karasu Uysal ⁷³, D. Karatovic ⁹⁰, O. Karavichev ¹⁴², T. Karavicheva ¹⁴², P. Karczmarczyk ¹³⁷, E. Karpechev ¹⁴², U. Kebschull ⁷¹, R. Keidel ¹⁴¹, D.L.D. Keijdener ⁶⁰, M. Keil ³³, B. Ketzer ⁴³, S.S. Khade ⁴⁹, A.M. Khan ^{121,6}, S. Khan ¹⁶, A. Khanzadeev ¹⁴², Y. Kharlov ¹⁴², A. Khatun ¹¹⁹, A. Khuntia ³⁶, B. Kileng ³⁵, B. Kim ¹⁰⁵, C. Kim ¹⁷, D.J. Kim ¹¹⁸, E.J. Kim ⁷⁰, J. Kim ¹⁴⁰, J.S. Kim ⁴¹, J. Kim ⁵⁹, J. Kim ⁷⁰, M. Kim ¹⁹, S. Kim ¹⁸, T. Kim ¹⁴⁰, K. Kimura ⁹³, S. Kirsch ⁶⁵, I. Kisiel ³⁹, S. Kiselev ¹⁴², A. Kisiel ¹³⁷, J.P. Kitowski ², J.L. Klay ⁵, J. Klein ³³, S. Klein ⁷⁵, C. Klein-Bösing ¹²⁷, M. Kleiner ⁶⁵, T. Klemenz ⁹⁶, A. Kluge ³³, A.G. Knospe ¹¹⁷, C. Kobdaj ¹⁰⁶, T. Kollegger ⁹⁸, A. Kondratyev ¹⁴³, N. Kondratyeva ¹⁴², E. Kondratyuk ¹⁴², J. Konig ⁶⁵, S.A. Konigstorfer ⁹⁶, P.J. Konopka ³³, G. Kornakov ¹³⁷, M. Kowwieser ⁹⁶, S.D. Koryciak ², A. Kotliarov ⁸⁷, V. Kovalenko ¹⁴², M. Kowalski ¹⁰⁸, V. Kozhuharov ³⁷, I. Králík ⁶¹, A. Kravčáková ³⁸, L. Krcal ^{33,39}, M. Krivda ^{101,61}, F. Krizek ⁸⁷, K. Krizkova Gajdosova ³³, M. Kroesen ⁹⁵, M. Krüger ⁶⁵, D.M. Krupova ³⁶, E. Kryshen ¹⁴², V. Kučera ⁵⁹, C. Kuhn ¹³⁰, P.G. Kuijer ⁸⁵, T. Kumaoka ¹²⁶, D. Kumar ¹³⁶, L. Kumar ⁹¹, N. Kumar ⁹¹, S. Kumar ³², S. Kundu ³³, P. Kurashvili ⁸⁰, A. Kurepin ¹⁴², A.B. Kurepin ¹⁴², A. Kuryakin ¹⁴², S. Kushpil ⁸⁷, M.J. Kweon ⁵⁹, Y. Kwon ¹⁴⁰, S.L. La Pointe ³⁹, P. La Rocca ²⁷, A. Lakrathok ¹⁰⁶, M. Lamanna ³³, A.R. Landou ^{74,116}, R. Langoy ¹²², P. Larionov ³³, E. Laudi ³³, L. Lautner ^{33,96}, R. Lavicka ¹⁰³, R. Lea ^{135,56}, H. Lee ¹⁰⁵, I. Legrand ⁴⁶, G. Legras ¹²⁷, J. Lehrbach ³⁹, T.M. Lelek ², R.C. Lemmon ⁸⁶, I. León Monzón ¹¹⁰, M.M. Lesch ⁹⁶, E.D. Lesser ¹⁹, P. Lévai ⁴⁷, X. Li ¹⁰, J. Lien ¹²², R. Lietava ¹⁰¹, I. Likmeta ¹¹⁷, B. Lim ²⁵, S.H. Lim ¹⁷, V. Lindenstruth ³⁹, A. Lindner ⁴⁶, C. Lippmann ⁹⁸, D.H. Liu ⁶, J. Liu ¹²⁰, G.S.S. Liveraro ¹¹², I.M. Lofnes ²¹, C. Loizides ⁸⁸, S. Lokos ¹⁰⁸, J. Lömkér ⁶⁰, P. Loncar ³⁴, X. Lopez ¹²⁸, E. López Torres ⁷, P. Lu ^{98,121}, F.V. Lugo ⁶⁸, J.R. Luhder ¹²⁷, M. Lunardon ²⁸, G. Luparello ⁵⁸, Y.G. Ma ⁴⁰, M. Mager ³³, A. Maire ¹³⁰, E.M. Majerz ², M.V. Makarieva ³⁷, M. Malaev ¹⁴², G. Malfattore ²⁶, N.M. Malik ⁹², Q.W. Malik ²⁰, S.K. Malik ⁹², L. Malinina ^{I,VII,143}, D. Mallick ^{132,81}, N. Mallick ⁴⁹, G. Mandaglio ^{31,54}, S.K. Mandal ⁸⁰, V. Manko ¹⁴², F. Manso ¹²⁸, V. Manzari ⁵¹, Y. Mao ⁶, R.W. Marcjan ², G.V. Margagliotti ²⁴, A. Margotti ⁵², A. Marín ⁹⁸, C. Markert ¹⁰⁹, P. Martinengo ³³, M.I. Martínez ⁴⁵, G. Martínez García ¹⁰⁴, M.P.P. Martins ¹¹¹, S. Masciocchi ⁹⁸, M. Masera ²⁵, A. Masoni ⁵³, L. Massacrier ¹³², O. Massen ⁶⁰, A. Mastroserio ^{133,51}, O. Matonoha ⁷⁶, S. Mattiazzzo ²⁸, A. Matyja ¹⁰⁸, C. Mayer ¹⁰⁸, A.L. Mazuecos ³³, F. Mazzaschi ²⁵, M. Mazzilli ³³, J.E. Mdhluli ¹²⁴, Y. Melikyan ⁴⁴, A. Menchaca-Rocha ⁶⁸, J.E.M. Mendez ⁶⁶, E. Meninno ¹⁰³, A.S. Menon ¹¹⁷, M. Meres ¹³, S. Mhlanga ^{115,69}, Y. Miake ¹²⁶, L. Micheletti ³³, D.L. Mihaylov ⁹⁶, K. Mikhaylov ^{143,142}, A.N. Mishra ⁴⁷, D. Miśkowiec ⁹⁸, A. Modak ⁴, B. Mohanty ⁸¹, M. Mohisin Khan ^{V,16}, M.A. Molander ⁴⁴, S. Monira ¹³⁷, C. Mordasini ¹¹⁸, D.A. Moreira De Godoy ¹²⁷, I. Morozov ¹⁴², A. Morsch ³³, T. Mrnjavac ³³, V. Muccifora ⁵⁰, S. Muhuri ¹³⁶, J.D. Mulligan ⁷⁵, A. Mulliri ²³, M.G. Munhoz ¹¹¹, R.H. Munzer ⁶⁵, H. Murakami ¹²⁵, S. Murray ¹¹⁵, L. Musa ³³, J. Musinsky ⁶¹, J.W. Myrcha ¹³⁷, B. Naik ¹²⁴, A.I. Nambrath ¹⁹, B.K. Nandi ⁴⁸, R. Nania ⁵², E. Nappi ⁵¹, A.F. Nassirpour ¹⁸, A. Nath ⁹⁵, C. Natrass ¹²³, M.N. Naydenov ³⁷, A. Neagu ²⁰, A. Negru ¹¹⁴, L. Nellen ⁶⁶, R. Nepeivoda ⁷⁶, S. Nese ²⁰, G. Neskovic ³⁹, N. Nicassio ⁵¹, B.S. Nielsen ⁸⁴, E.G. Nielsen ⁸⁴, S. Nikolaev ¹⁴², S. Nikulin ¹⁴², V. Nikulin ¹⁴², F. Noferini ⁵², S. Noh ¹², P. Nomokonov ¹⁴³, J. Norman ¹²⁰, N. Novitzky ⁸⁸, P. Nowakowski ¹³⁷, A. Nyandin ¹⁴², J. Nystrand ²¹, M. Ogino ⁷⁷, S. Oh ¹⁸, A. Ohlson ⁷⁶, V.A. Okorokov ¹⁴², J. Oleniacz ¹³⁷, A.C. Oliveira Da Silva ¹²³, A. Onnerstad ¹¹⁸, C. Oppedisano ⁵⁷, A. Ortiz Velasquez ⁶⁶, J. Otwinowski ¹⁰⁸, M. Oya ⁹³, K. Oyama ⁷⁷, Y. Pachmayer ⁹⁵, S. Padhan ⁴⁸, D. Pagano ^{135,56}, G. Paić ⁶⁶, S. Paisano-Guzmán ⁴⁵, A. Palasciano ⁵¹,

- S. Panebianco ¹³¹, H. Park ¹²⁶, H. Park ¹⁰⁵, J. Park ⁵⁹, J.E. Parkkila ³³, Y. Patley ⁴⁸, R.N. Patra⁹²,
 B. Paul ²³, H. Pei ⁶, T. Peitzmann ⁶⁰, X. Peng ¹¹, M. Pennisi ²⁵, S. Perciballi ²⁵, D. Peresunko ¹⁴²,
 G.M. Perez ⁷, Y. Pestov¹⁴², V. Petrov ¹⁴², M. Petrovici ⁴⁶, R.P. Pezzi ^{104,67}, S. Piano ⁵⁸, M. Pikna ¹³,
 P. Pillot ¹⁰⁴, O. Pinazza ^{52,33}, L. Pinsky¹¹⁷, C. Pinto ⁹⁶, S. Pisano ⁵⁰, M. Płoskoń ⁷⁵, M. Planinic⁹⁰,
 F. Pliquet⁶⁵, M.G. Poghosyan ⁸⁸, B. Polichtchouk ¹⁴², S. Politano ³⁰, N. Poljak ⁹⁰, A. Pop ⁴⁶,
 S. Porteboeuf-Houssais ¹²⁸, V. Pozdniakov ¹⁴³, I.Y. Pozos ⁴⁵, K.K. Pradhan ⁴⁹, S.K. Prasad ⁴,
 S. Prasad ⁴⁹, R. Preghenella ⁵², F. Prino ⁵⁷, C.A. Pruneau ¹³⁸, I. Pshenichnov ¹⁴², M. Puccio ³³,
 S. Pucillo ²⁵, Z. Pugelova¹⁰⁷, S. Qiu ⁸⁵, L. Quaglia ²⁵, S. Ragoni ¹⁵, A. Rai ¹³⁹,
 A. Rakotozafindrabe ¹³¹, L. Ramello ^{134,57}, F. Rami ¹³⁰, T.A. Rancien ⁷⁴, M. Rasa ²⁷, S.S. Räsänen ⁴⁴,
 R. Rath ⁵², M.P. Rauch ²¹, I. Ravasenga ⁸⁵, K.F. Read ^{88,123}, C. Reckziegel ¹¹³, A.R. Redelbach ³⁹,
 K. Redlich ^{VI,80}, C.A. Reetz ⁹⁸, H.D. Regules-Medel⁴⁵, A. Rehman²¹, F. Reidt ³³, H.A. Reme-Ness ³⁵,
 Z. Rescakova³⁸, K. Reygers ⁹⁵, A. Riabov ¹⁴², V. Riabov ¹⁴², R. Ricci ²⁹, M. Richter ²⁰,
 A.A. Riedel ⁹⁶, W. Riegler ³³, A.G. Rifferto ²⁵, C. Ristea ⁶⁴, M.V. Rodriguez ³³, M. Rodríguez
 Cahuantzi ⁴⁵, S.A. Rodríguez Ramírez ⁴⁵, K. Røed ²⁰, R. Rogalev ¹⁴², E. Rogochaya ¹⁴³,
 T.S. Rogoschinski ⁶⁵, D. Rohr ³³, D. Röhrich ²¹, P.F. Rojas⁴⁵, S. Rojas Torres ³⁶, P.S. Rokita ¹³⁷,
 G. Romanenko ²⁶, F. Ronchetti ⁵⁰, A. Rosano ^{31,54}, E.D. Rosas⁶⁶, K. Roslon ¹³⁷, A. Rossi ⁵⁵,
 A. Roy ⁴⁹, S. Roy ⁴⁸, N. Rubini ²⁶, D. Ruggiano ¹³⁷, R. Rui ²⁴, P.G. Russek ², R. Russo ⁸⁵,
 A. Rustamov ⁸², E. Ryabinkin ¹⁴², Y. Ryabov ¹⁴², A. Rybicki ¹⁰⁸, H. Rytkonen ¹¹⁸, J. Ryu ¹⁷,
 W. Rzesz ¹³⁷, O.A.M. Saarimaki ⁴⁴, S. Sadhu ³², S. Sadovsky ¹⁴², J. Saetre ²¹, K. Šafářík ³⁶, P. Saha⁴²,
 S.K. Saha ⁴, S. Saha ⁸¹, B. Sahoo ⁴⁸, B. Sahoo ⁴⁹, R. Sahoo ⁴⁹, S. Sahoo⁶², D. Sahu ⁴⁹, P.K. Sahu ⁶²,
 J. Saini ¹³⁶, K. Sajdakova³⁸, S. Sakai ¹²⁶, M.P. Salvan ⁹⁸, S. Sambyal ⁹², D. Samitz ¹⁰³, I. Sanna ^{33,96},
 T.B. Saramela¹¹¹, P. Sarma ⁴², V. Sarritzu ²³, V.M. Sarti ⁹⁶, M.H.P. Sas ¹³⁹, S. Sawan⁸¹, J. Schambach ⁸⁸,
 H.S. Scheid ⁶⁵, C. Schiaua ⁴⁶, R. Schicker ⁹⁵, A. Schmeh⁹⁸, C. Schmidt ⁹⁸, H.R. Schmidt⁹⁴,
 M.O. Schmidt ³³, M. Schmidt⁹⁴, N.V. Schmidt ⁸⁸, A.R. Schmier ¹²³, R. Schotter ¹³⁰, A. Schröter ³⁹,
 J. Schukraft ³³, K. Schweda ⁹⁸, G. Scioli ²⁶, E. Scomparin ⁵⁷, J.E. Seger ¹⁵, Y. Sekiguchi¹²⁵,
 D. Sekihata ¹²⁵, M. Selina ⁸⁵, I. Selyuzhenkov ⁹⁸, S. Senyukov ¹³⁰, J.J. Seo ^{95,59}, D. Serebryakov ¹⁴²,
 L. Šerkšnytė ⁹⁶, A. Sevcenco ⁶⁴, T.J. Shaba ⁶⁹, A. Shabetai ¹⁰⁴, R. Shahoyan³³, A. Shangaraev ¹⁴²,
 A. Sharma⁹¹, B. Sharma ⁹², D. Sharma ⁴⁸, H. Sharma ^{55,108}, M. Sharma ⁹², S. Sharma ⁷⁷, S. Sharma ⁹²,
 U. Sharma ⁹², A. Shatat ¹³², O. Sheibani¹¹⁷, K. Shigaki ⁹³, M. Shimomura⁷⁸, J. Shin¹², S. Shirinkin ¹⁴²,
 Q. Shou ⁴⁰, Y. Sibirjak ¹⁴², S. Siddhanta ⁵³, T. Siemiarczuk ⁸⁰, T.F. Silva ¹¹¹, D. Silvermyr ⁷⁶,
 T. Simantathammakul¹⁰⁶, R. Simeonov ³⁷, B. Singh⁹², B. Singh ⁹⁶, K. Singh ⁴⁹, R. Singh ⁸¹, R. Singh ⁹²,
 R. Singh ⁴⁹, S. Singh ¹⁶, V.K. Singh ¹³⁶, V. Singhal ¹³⁶, T. Sinha ¹⁰⁰, B. Sitar ¹³, M. Sitta ^{134,57},
 T.B. Skaali²⁰, G. Skorodumovs ⁹⁵, M. Slupecki ⁴⁴, N. Smirnov ¹³⁹, R.J.M. Snellings ⁶⁰, E.H. Solheim ²⁰,
 J. Song ¹⁷, C. Sonnabend ^{33,98}, F. Soramel ²⁸, A.B. Soto-hernandez ⁸⁹, R. Spijkers ⁸⁵, I. Sputowska ¹⁰⁸,
 J. Staa ⁷⁶, J. Stachel ⁹⁵, I. Stan ⁶⁴, P.J. Steffanici ¹²³, S.F. Stiefelmaier ⁹⁵, D. Stocco ¹⁰⁴,
 I. Storehaug ²⁰, P. Stratmann ¹²⁷, S. Strazzi ²⁶, A. Sturniolo ^{31,54}, C.P. Stylianidis⁸⁵, A.A.P. Suade ¹¹¹,
 C. Suire ¹³², M. Sukhanov ¹⁴², M. Suljic ³³, R. Sultanov ¹⁴², V. Sumberia ⁹², S. Sumowidagdo ⁸³,
 S. Swain⁶², I. Szarka ¹³, M. Szymkowski ¹³⁷, S.F. Taghavi ⁹⁶, G. Taillepied ⁹⁸, J. Takahashi ¹¹²,
 G.J. Tambave ⁸¹, S. Tang ⁶, Z. Tang ¹²¹, J.D. Tapia Takaki ¹¹⁹, N. Tapus¹¹⁴, L.A. Tarasovicova ¹²⁷,
 M.G. Tarzila ⁴⁶, G.F. Tassielli ³², A. Tauro ³³, A. Tavira García ¹³², G. Tejeda Muñoz ⁴⁵, A. Telesca ³³,
 L. Terlizzi ²⁵, C. Terrevoli ¹¹⁷, S. Thakur ⁴, D. Thomas ¹⁰⁹, A. Tikhonov ¹⁴², A.R. Timmins ¹¹⁷,
 M. Tkacik¹⁰⁷, T. Tkacik ¹⁰⁷, A. Toia ⁶⁵, R. Tokumoto⁹³, K. Tomohiro⁹³, N. Topilskaya ¹⁴², M. Toppi ⁵⁰,
 T. Tork ¹³², V.V. Torres ¹⁰⁴, A.G. Torres Ramos ³², A. Trifiró ^{31,54}, A.S. Triolo ^{33,31,54}, S. Tripathy ⁵²,
 T. Tripathy ⁴⁸, S. Trogolo ³³, V. Trubnikov ³, W.H. Trzaska ¹¹⁸, T.P. Trzcinski ¹³⁷, A. Tumkin ¹⁴²,
 R. Turrisi ⁵⁵, T.S. Tveter ²⁰, K. Ullaland ²¹, B. Ulukutlu ⁹⁶, A. Uras ¹²⁹, G.L. Usai ²³, M. Vala³⁸,
 N. Valle ²², L.V.R. van Doremalen⁶⁰, M. van Leeuwen ⁸⁵, C.A. van Veen ⁹⁵, R.J.G. van Weelden ⁸⁵,
 P. Vande Vyvre ³³, D. Varga ⁴⁷, Z. Varga ⁴⁷, M. Vasileiou ⁷⁹, A. Vasiliev ¹⁴², O. Vázquez Doce ⁵⁰,
 O. Vazquez Rueda ¹¹⁷, V. Vechernin ¹⁴², E. Vercellin ²⁵, S. Vergara Limón⁴⁵, R. Verma⁴⁸, L. Vermunt ⁹⁸,
 R. Vértesi ⁴⁷, M. Verweij ⁶⁰, L. Vickovic³⁴, Z. Vilakazi¹²⁴, O. Villalobos Baillie ¹⁰¹, A. Villani ²⁴,
 A. Vinogradov ¹⁴², T. Virgili ²⁹, M.M.O. Virta ¹¹⁸, V. Vislavicius⁷⁶, A. Vodopyanov ¹⁴³, B. Volkel ³³,
 M.A. Völkl ⁹⁵, K. Voloshin ¹⁴², S.A. Voloshin ¹³⁸, G. Volpe ³², B. von Haller ³³, I. Vorobyev ⁹⁶,
 N. Vozniuk ¹⁴², J. Vrláková ³⁸, J. Wan⁴⁰, C. Wang ⁴⁰, D. Wang ⁴⁰, Y. Wang ⁴⁰, Y. Wang ⁶,
 A. Wegrzynek ³³, F.T. Weiglhofer³⁹, S.C. Wenzel ³³, J.P. Wessels ¹²⁷, J. Wiechula ⁶⁵, J. Wikne ²⁰,
 G. Wilk ⁸⁰, J. Wilkinson ⁹⁸, G.A. Willems ¹²⁷, B. Windelband ⁹⁵, M. Winn ¹³¹, J.R. Wright ¹⁰⁹,
 W. Wu⁴⁰, Y. Wu ¹²¹, R. Xu ⁶, A. Yadav ⁴³, A.K. Yadav ¹³⁶, S. Yalcin ⁷³, Y. Yamaguchi ⁹³, S. Yang²¹,
 S. Yano ⁹³, Z. Yin ⁶, I.-K. Yoo ¹⁷, J.H. Yoon ⁵⁹, H. Yu¹², S. Yuan²¹, A. Yuncu ⁹⁵, V. Zaccolo ²⁴,

C. Zampolli ³³, F. Zanone ⁹⁵, N. Zardoshti ³³, A. Zarochentsev ¹⁴², P. Závada ⁶³, N. Zaviyalov ¹⁴², M. Zhalov ¹⁴², B. Zhang ⁶, C. Zhang ¹³¹, L. Zhang ⁴⁰, S. Zhang ⁴⁰, X. Zhang ⁶, Y. Zhang ¹²¹, Z. Zhang ⁶, M. Zhao ¹⁰, V. Zhrebchevskii ¹⁴², Y. Zhi ¹⁰, D. Zhou ⁶, Y. Zhou ⁸⁴, J. Zhu ^{55,6}, Y. Zhu ⁶, S.C. Zugravil ⁵⁷, N. Zurlo ^{135,56}

Affiliation Notes

^I Deceased

^{II} Also at: Max-Planck-Institut für Physik, Munich, Germany

^{III} Also at: Italian National Agency for New Technologies, Energy and Sustainable Economic Development (ENEA), Bologna, Italy

^{IV} Also at: Dipartimento DET del Politecnico di Torino, Turin, Italy

^V Also at: Department of Applied Physics, Aligarh Muslim University, Aligarh, India

^{VI} Also at: Institute of Theoretical Physics, University of Wrocław, Poland

^{VII} Also at: An institution covered by a cooperation agreement with CERN

Collaboration Institutes

¹ A.I. Alikhanyan National Science Laboratory (Yerevan Physics Institute) Foundation, Yerevan, Armenia

² AGH University of Krakow, Cracow, Poland

³ Bogolyubov Institute for Theoretical Physics, National Academy of Sciences of Ukraine, Kiev, Ukraine

⁴ Bose Institute, Department of Physics and Centre for Astroparticle Physics and Space Science (CAPSS), Kolkata, India

⁵ California Polytechnic State University, San Luis Obispo, California, United States

⁶ Central China Normal University, Wuhan, China

⁷ Centro de Aplicaciones Tecnológicas y Desarrollo Nuclear (CEADEN), Havana, Cuba

⁸ Centro de Investigación y de Estudios Avanzados (CINVESTAV), Mexico City and Mérida, Mexico

⁹ Chicago State University, Chicago, Illinois, United States

¹⁰ China Institute of Atomic Energy, Beijing, China

¹¹ China University of Geosciences, Wuhan, China

¹² Chungbuk National University, Cheongju, Republic of Korea

¹³ Comenius University Bratislava, Faculty of Mathematics, Physics and Informatics, Bratislava, Slovak Republic

¹⁴ COMSATS University Islamabad, Islamabad, Pakistan

¹⁵ Creighton University, Omaha, Nebraska, United States

¹⁶ Department of Physics, Aligarh Muslim University, Aligarh, India

¹⁷ Department of Physics, Pusan National University, Pusan, Republic of Korea

¹⁸ Department of Physics, Sejong University, Seoul, Republic of Korea

¹⁹ Department of Physics, University of California, Berkeley, California, United States

²⁰ Department of Physics, University of Oslo, Oslo, Norway

²¹ Department of Physics and Technology, University of Bergen, Bergen, Norway

²² Dipartimento di Fisica, Università di Pavia, Pavia, Italy

²³ Dipartimento di Fisica dell’Università and Sezione INFN, Cagliari, Italy

²⁴ Dipartimento di Fisica dell’Università and Sezione INFN, Trieste, Italy

²⁵ Dipartimento di Fisica dell’Università and Sezione INFN, Turin, Italy

²⁶ Dipartimento di Fisica e Astronomia dell’Università and Sezione INFN, Bologna, Italy

²⁷ Dipartimento di Fisica e Astronomia dell’Università and Sezione INFN, Catania, Italy

²⁸ Dipartimento di Fisica e Astronomia dell’Università and Sezione INFN, Padova, Italy

²⁹ Dipartimento di Fisica ‘E.R. Caianiello’ dell’Università and Gruppo Collegato INFN, Salerno, Italy

³⁰ Dipartimento DISAT del Politecnico and Sezione INFN, Turin, Italy

³¹ Dipartimento di Scienze MIFT, Università di Messina, Messina, Italy

³² Dipartimento Interateneo di Fisica ‘M. Merlin’ and Sezione INFN, Bari, Italy

³³ European Organization for Nuclear Research (CERN), Geneva, Switzerland

³⁴ Faculty of Electrical Engineering, Mechanical Engineering and Naval Architecture, University of Split, Split, Croatia

³⁵ Faculty of Engineering and Science, Western Norway University of Applied Sciences, Bergen, Norway

- ³⁶ Faculty of Nuclear Sciences and Physical Engineering, Czech Technical University in Prague, Prague, Czech Republic
³⁷ Faculty of Physics, Sofia University, Sofia, Bulgaria
³⁸ Faculty of Science, P.J. Šafárik University, Košice, Slovak Republic
³⁹ Frankfurt Institute for Advanced Studies, Johann Wolfgang Goethe-Universität Frankfurt, Frankfurt, Germany
⁴⁰ Fudan University, Shanghai, China
⁴¹ Gangneung-Wonju National University, Gangneung, Republic of Korea
⁴² Gauhati University, Department of Physics, Guwahati, India
⁴³ Helmholtz-Institut für Strahlen- und Kernphysik, Rheinische Friedrich-Wilhelms-Universität Bonn, Bonn, Germany
⁴⁴ Helsinki Institute of Physics (HIP), Helsinki, Finland
⁴⁵ High Energy Physics Group, Universidad Autónoma de Puebla, Puebla, Mexico
⁴⁶ Horia Hulubei National Institute of Physics and Nuclear Engineering, Bucharest, Romania
⁴⁷ HUN-REN Wigner Research Centre for Physics, Budapest, Hungary
⁴⁸ Indian Institute of Technology Bombay (IIT), Mumbai, India
⁴⁹ Indian Institute of Technology Indore, Indore, India
⁵⁰ INFN, Laboratori Nazionali di Frascati, Frascati, Italy
⁵¹ INFN, Sezione di Bari, Bari, Italy
⁵² INFN, Sezione di Bologna, Bologna, Italy
⁵³ INFN, Sezione di Cagliari, Cagliari, Italy
⁵⁴ INFN, Sezione di Catania, Catania, Italy
⁵⁵ INFN, Sezione di Padova, Padova, Italy
⁵⁶ INFN, Sezione di Pavia, Pavia, Italy
⁵⁷ INFN, Sezione di Torino, Turin, Italy
⁵⁸ INFN, Sezione di Trieste, Trieste, Italy
⁵⁹ Inha University, Incheon, Republic of Korea
⁶⁰ Institute for Gravitational and Subatomic Physics (GRASP), Utrecht University/Nikhef, Utrecht, Netherlands
⁶¹ Institute of Experimental Physics, Slovak Academy of Sciences, Košice, Slovak Republic
⁶² Institute of Physics, Homi Bhabha National Institute, Bhubaneswar, India
⁶³ Institute of Physics of the Czech Academy of Sciences, Prague, Czech Republic
⁶⁴ Institute of Space Science (ISS), Bucharest, Romania
⁶⁵ Institut für Kernphysik, Johann Wolfgang Goethe-Universität Frankfurt, Frankfurt, Germany
⁶⁶ Instituto de Ciencias Nucleares, Universidad Nacional Autónoma de México, Mexico City, Mexico
⁶⁷ Instituto de Física, Universidade Federal do Rio Grande do Sul (UFRGS), Porto Alegre, Brazil
⁶⁸ Instituto de Física, Universidad Nacional Autónoma de México, Mexico City, Mexico
⁶⁹ iThemba LABS, National Research Foundation, Somerset West, South Africa
⁷⁰ Jeonbuk National University, Jeonju, Republic of Korea
⁷¹ Johann-Wolfgang-Goethe Universität Frankfurt Institut für Informatik, Fachbereich Informatik und Mathematik, Frankfurt, Germany
⁷² Korea Institute of Science and Technology Information, Daejeon, Republic of Korea
⁷³ KTO Karatay University, Konya, Turkey
⁷⁴ Laboratoire de Physique Subatomique et de Cosmologie, Université Grenoble-Alpes, CNRS-IN2P3, Grenoble, France
⁷⁵ Lawrence Berkeley National Laboratory, Berkeley, California, United States
⁷⁶ Lund University Department of Physics, Division of Particle Physics, Lund, Sweden
⁷⁷ Nagasaki Institute of Applied Science, Nagasaki, Japan
⁷⁸ Nara Women's University (NWU), Nara, Japan
⁷⁹ National and Kapodistrian University of Athens, School of Science, Department of Physics , Athens, Greece
⁸⁰ National Centre for Nuclear Research, Warsaw, Poland
⁸¹ National Institute of Science Education and Research, Homi Bhabha National Institute, Jatni, India
⁸² National Nuclear Research Center, Baku, Azerbaijan
⁸³ National Research and Innovation Agency - BRIN, Jakarta, Indonesia
⁸⁴ Niels Bohr Institute, University of Copenhagen, Copenhagen, Denmark
⁸⁵ Nikhef, National institute for subatomic physics, Amsterdam, Netherlands
⁸⁶ Nuclear Physics Group, STFC Daresbury Laboratory, Daresbury, United Kingdom
⁸⁷ Nuclear Physics Institute of the Czech Academy of Sciences, Husinec-Řež, Czech Republic

- ⁸⁸ Oak Ridge National Laboratory, Oak Ridge, Tennessee, United States
⁸⁹ Ohio State University, Columbus, Ohio, United States
⁹⁰ Physics department, Faculty of science, University of Zagreb, Zagreb, Croatia
⁹¹ Physics Department, Panjab University, Chandigarh, India
⁹² Physics Department, University of Jammu, Jammu, India
⁹³ Physics Program and International Institute for Sustainability with Knotted Chiral Meta Matter (SKCM2), Hiroshima University, Hiroshima, Japan
⁹⁴ Physikalischs Institut, Eberhard-Karls-Universität Tübingen, Tübingen, Germany
⁹⁵ Physikalischs Institut, Ruprecht-Karls-Universität Heidelberg, Heidelberg, Germany
⁹⁶ Physik Department, Technische Universität München, Munich, Germany
⁹⁷ Politecnico di Bari and Sezione INFN, Bari, Italy
⁹⁸ Research Division and ExtreMe Matter Institute EMMI, GSI Helmholtzzentrum für Schwerionenforschung GmbH, Darmstadt, Germany
⁹⁹ Saga University, Saga, Japan
¹⁰⁰ Saha Institute of Nuclear Physics, Homi Bhabha National Institute, Kolkata, India
¹⁰¹ School of Physics and Astronomy, University of Birmingham, Birmingham, United Kingdom
¹⁰² Sección Física, Departamento de Ciencias, Pontificia Universidad Católica del Perú, Lima, Peru
¹⁰³ Stefan Meyer Institut für Subatomare Physik (SMI), Vienna, Austria
¹⁰⁴ SUBATECH, IMT Atlantique, Nantes Université, CNRS-IN2P3, Nantes, France
¹⁰⁵ Sungkyunkwan University, Suwon City, Republic of Korea
¹⁰⁶ Suranaree University of Technology, Nakhon Ratchasima, Thailand
¹⁰⁷ Technical University of Košice, Košice, Slovak Republic
¹⁰⁸ The Henryk Niewodniczanski Institute of Nuclear Physics, Polish Academy of Sciences, Cracow, Poland
¹⁰⁹ The University of Texas at Austin, Austin, Texas, United States
¹¹⁰ Universidad Autónoma de Sinaloa, Culiacán, Mexico
¹¹¹ Universidade de São Paulo (USP), São Paulo, Brazil
¹¹² Universidade Estadual de Campinas (UNICAMP), Campinas, Brazil
¹¹³ Universidade Federal do ABC, Santo Andre, Brazil
¹¹⁴ Universitatea Nationala de Stiinta si Tehnologie Politehnica Bucuresti, Bucharest, Romania
¹¹⁵ University of Cape Town, Cape Town, South Africa
¹¹⁶ University of Derby, Derby, United Kingdom
¹¹⁷ University of Houston, Houston, Texas, United States
¹¹⁸ University of Jyväskylä, Jyväskylä, Finland
¹¹⁹ University of Kansas, Lawrence, Kansas, United States
¹²⁰ University of Liverpool, Liverpool, United Kingdom
¹²¹ University of Science and Technology of China, Hefei, China
¹²² University of South-Eastern Norway, Kongsberg, Norway
¹²³ University of Tennessee, Knoxville, Tennessee, United States
¹²⁴ University of the Witwatersrand, Johannesburg, South Africa
¹²⁵ University of Tokyo, Tokyo, Japan
¹²⁶ University of Tsukuba, Tsukuba, Japan
¹²⁷ Universität Münster, Institut für Kernphysik, Münster, Germany
¹²⁸ Université Clermont Auvergne, CNRS/IN2P3, LPC, Clermont-Ferrand, France
¹²⁹ Université de Lyon, CNRS/IN2P3, Institut de Physique des 2 Infinis de Lyon, Lyon, France
¹³⁰ Université de Strasbourg, CNRS, IPHC UMR 7178, F-67000 Strasbourg, France, Strasbourg, France
¹³¹ Université Paris-Saclay, Centre d'Etudes de Saclay (CEA), IRFU, Département de Physique Nucléaire (DPhN), Saclay, France
¹³² Université Paris-Saclay, CNRS/IN2P3, IJCLab, Orsay, France
¹³³ Università degli Studi di Foggia, Foggia, Italy
¹³⁴ Università del Piemonte Orientale, Vercelli, Italy
¹³⁵ Università di Brescia, Brescia, Italy
¹³⁶ Variable Energy Cyclotron Centre, Homi Bhabha National Institute, Kolkata, India
¹³⁷ Warsaw University of Technology, Warsaw, Poland
¹³⁸ Wayne State University, Detroit, Michigan, United States
¹³⁹ Yale University, New Haven, Connecticut, United States
¹⁴⁰ Yonsei University, Seoul, Republic of Korea

¹⁴¹ Zentrum für Technologie und Transfer (ZTT), Worms, Germany

¹⁴² Affiliated with an institute covered by a cooperation agreement with CERN

¹⁴³ Affiliated with an international laboratory covered by a cooperation agreement with CERN.